Quantification of Fuel Chemistry Effects on Burning Modes in Turbulent Premixed Flames

F. Hampp*, R. P. Lindstedt**

Department of Mechanical Engineering, Imperial College, London, SW7 2AZ, UK

Abstract

The present work quantifies the impact of fuel chemistry on burning modes using premixed dimethyl ether (DME), ethanol (EtOH) and methane flames in a back-to-burnt opposed jet configuration. The study considers equivalence ratios $0 \leq \Phi \leq 1$, resulting in a Damköhler (Da) number range $0.06 \leq Da \leq 5.1$. Multi-scale turbulence ($Re \simeq 19{,}550$ and $Re_t \simeq 360$) is generated by means of a cross fractal grid and kept constant along with the enthalpy of the hot combustion products (T_{HCP} = 1700 K) of the counterflow stream. The mean turbulent rate of strain exceeds the laminar extinction rate for all flames. Simultaneous Mie scattering, OH-PLIF and PIV are used to identify reactants, mixing, weakly reacting, strongly reacting and product fluids. The relative balance between conventional flame propagation and auto-ignition based combustion is highlighted using suitably defined Da numbers and a more rapid transition towards self-sustained (e.g. flamelet type) combustion is observed for DME. The strain rate distribution on the reactant fluid surface for methane remains similar to the (non-reactive) mixing layer ($\Phi = 0$), while DME and EtOH flames gradually detach from the stagnation plane with increasing Φ leading to stabilisation in regions with lower compressive rates of strain. The study further provides information on the conditions leading to burning mode transitions via (i) multi-fluid probabilities, (ii) structural flow field information and turbulence-flame interactions delineated by means of conditional (iii) velocity statistics and (iv) the rate of strain along fluid iso-contours.

Keywords: Turbulent Premixed Flames, Multi–Fluid Statistics, Fuel Effects, Combustion Chemistry, Damköhler Number Scaling

*Current address: Institute of Combustion Technology, German Aerospace Center (DLR), 70569 Stuttgart, Germany

**Corresponding author: Contact number +44 207 594 7039.
Email address: p.lindstedt@imperial.ac.uk (R. P. Lindstedt)

Nomenclature

Roman Letters

a	Rate of strain [s^{-1}].
$\overline{c}$	Reaction progress variable [–].
c	Progress variable; Instantaneous conditioning variable [–].
D	Burner nozzle diameter [m].
Da	Conventional Damköhler number [–].
Da_{ai}	Turbulent auto–ignition Damköhler number [–].
$d_{p,x}$	Al_2O_3 particle diameter x% [m].
e	Strain rate tensor [s^{-1}].
f	Rotated strain rate tensor [s^{-1}].
H	Burner nozzle separation [m].
I	Experimental fluorescence signal intensities [–].
$I^{\ddagger}$	Reference signal intensity [–].
Ka	Conventional Karlovitz number [–].
[k]	Theoretical concentration of species k [mol m^{-3}].
L_η	Kolmogorov length scale [m].
L_λ	Taylor microscale [m].
L_I	Integral length scale of turbulence [m].
M	Mixing fluid material surface [–].
N	Total number of images [–].
n	Instantaneous image [–].
$\hat{\mathbf{n}}$	Unit vector of the iso-contour normal [–].
$\dot{Q}$	Heat release rate [W m^{-3}].
Re	Reynolds number [–].
Re_λ	Reynolds number based on Taylor scales [–].
Re_t	Turbulent Reynolds number [–].
R	Reactant fluid material surface [–].
$\mathbf{R}$	Rotation matrix [–].
S	Strongly reacting fluid material surface [–].
S_L	Laminar burning velocity [m s^{-1}].
$\hat{\mathbf{s}}$	Unit vector of the streamline tangent [–].
T	Temperature [K].
T_{ad}	Adiabatic flame temperature [K].
T_{ai}	Auto–ignition temperature [K].
T_{HCP}	Hot combustion product temperature [K].
T_r	Reactant temperature [K].
$\underline{U}$	Flow velocity [m s^{-1}].
$\overline{U}$	Mean unconditional axial velocity [m s^{-1}].
$\overline{U_{\cdots}}$	Mean conditional axial velocity [m s^{-1}].
u	Axial velocity component [m s^{-1}].
$\overline{u^*}$	Leading edge velocity [m s^{-1}].
$\sqrt{u'^2}$	Unconditional axial velocity fluctuation [m s^{-1}].
$\sqrt{u'^2_{\cdots}}$	Conditional axial velocity fluctuation [m s^{-1}].
u_{rms}	Root mean square velocity fluctuation [m s^{-1}].
$\dot{V}_{\cdots}$	Volumetric flow rate [m^3 s^{-1}].
v	Radial velocity component [m s^{-1}].
$\sqrt{v'^2}$	Unconditional radial velocity fluctuation [m s^{-1}].
$\sqrt{v'^2_{\cdots}}$	Conditional radial velocity fluctuation [m s^{-1}].
W	Weakly reacting fluid material surface [–].

x	Axial coordinate [m].
x_s	Distance from origin of first thermal alteration [m].
y	Radial coordinate [m].

Greek Letters

β	Material surface iso-contour [–].
δ_f	Laminar fuel consumption layer thickness [m].
δ_l	Distance between the flame edge and the stagnation plane [m].
ε_r	Rate of dissipation in the reactants [m^2 s^{-3}].
Λ	Threshold value [–].
λ_B	Batchelor scale [m].
λ_D	Mean scalar dissipation layer thickness [m].
λ_{MF}	Multi–fluid spatial resolution [m].
λ_{PIV}	PIV spatial resolution [m].
ν_r	Reactants kinematic viscosity [m^2 s^{-1}].
Φ	Equivalence ratio [–].
Θ	Angle of rotation [°].
τ_c	Chemical timescale [s].
τ_η	Kolmogorov timescale [s].
τ_{ai}	Auto–ignition delay time [s].
τ_I	Integral timescale of turbulence [s].
ω	Vorticity [s^{-1}].

Sub/super-scripts

0	Alignment at the origin; Initial value.
Φ	Dependency on equivalence ratio.
‡	Reference value.
BTB	Back–to–burnt configuration.
b	Bulk flow motion.
d	Total.
FS	Fluid state.
I	Integral scale; Turbulent.
HCP	Hot combustion products.
i, j	Pixel index.
k	Velocity component.
LN	Lower nozzle.
m	Mixing fluid.
NE	Nozzle exit.
n	Instantaneous image; Normal component.
p	Product fluid.
q	Extinction conditions.
r	Reactant fluid.
s	Strongly reacting (flamelet) fluid.
T	Turbulent.
t	Tangential component.
UN	Upper nozzle.
w	Weakly reacting fluid.

1. Introduction

Novel combustion devices increasingly operate in the absence of distinct flame fronts, e.g. via distributed or flameless combustion modes, to fulfil increasingly stringent regulations on NOx and particulate emissions [1]. The approach has potentially significant advantages in terms of reduced emissions and improved fuel efficiency resulting in increased range. The operating conditions often exceed conventional extinction criteria and require thermal support, e.g. from exhaust gases [2], for sustained chemical activity. Practical examples that realise stable fuel-lean operation at low Damköhler numbers (Da) include flameless oxidation gas turbine engines [3] and industrial furnaces [4]. Minamoto et al. [5] investigated the reaction zone structure under flamelet and moderate or intense low-oxygen dilution (MILD) conditions using direct numerical simulation (DNS). The data showed the coexistence of thin and fragmented flamelets with spatially distributed chemical reactions. The broadening or fragmentation of a reaction zone is strongly dependent on the chemical timescale. The flamelet assumption is valid with reasonable accuracy for Karlovitz numbers (Ka) < 10 [6]. A mixture with low reactivity (e.g. low equivalence ratios or high dilution) requires substantially reduced turbulence [7] to move the reaction zone away from a bimodal structure, i.e. the spatial extent of intermediate products becomes statistically relevant. The blending of hot diluents with very fuel rich or lean mixtures can lead to conditions where the chemical timescale dominates the interaction with the turbulent flow [8] and, accordingly, the combustion chemistry assumes a decisive role [5, 6, 9]. Duwig et al. [10] investigated reaction zone broadening of vitiated methane/air jet flame with significant differences for lean (Φ = 0.4, 0.8) and rich ($\Phi = 6.0$) conditions observed. A deep penetration of the

CH and HCO radicals into the OH layer as well as a CH layer broadening of up to an order of magnitude compared to the laminar thickness was observed by Zhou et al. [7, 11–13]. Goh et al. [14] investigated the transition to flameless oxidation of fuel lean premixed JP-10 (exotetrahydrodicyclopentadiene) flames using a back-to-burnt (BTB) opposed jet configuration and compared results to corresponding twin flames approaching extinction [15]. Hampp and Lindstedt [16, 17] found that high Da counterflow flames detach from the stagnation plane and anchor in low compressive strain regions. Such flames exhibit a clear flamelet-like structure with steep scalar gradients and a distinct dilatation direction. By contrast, low Da combustion precluded conventional flame propagation leading to strong deviations from bimodal structures and OH gradients well below the (theoretical) flamelet limit due to turbulent transport. Reaction progress can also become increasingly dependent on external enthalpy sources [18, 19].

External enthalpy stabilised combustion exhibits complex turbulence–chemistry interactions that may lead to a competition between auto-ignition related oxidation and conventional flame propagation [17, 20]. While laminar burning properties of many hydrocarbon fuels are similar, the auto-ignition delay time can vary by orders of magnitude. Consequently, fuel chemistry effects come to the fore under low Da conditions, yet there is a lack of understanding of the associated turbulence – chemistry interactions. Sabia et al. [21, 22] investigated propane auto-ignition for a wide range of MILD conditions and noted a strong inert gas dilution effect. Fuel lean pre–vaporised acetone, ethanol and n-heptane were investigated by Ye et al. [23] in a MILD combustor with distinct differences in flame stability observed. Wang et al. [24, 25] explored the extinction characteristics of premixed and non-premixed DME and ethanol (EtOH) flames in an opposed jet geometry

with DME showing a higher strain resilience than EtOH.

The present study quantifies the impact of combustion chemistry on burning mode transitions by the use of DME, EtOH and CH_4 over a wide range of Karlovitz ($3.3 \cdot 10^{-3} \leq Ka^{-1} \leq 0.27$) and Damköhler ($6.0 \cdot 10^{-2} \leq Da \leq 5.1$) numbers using an opposed jet configuration. The chemical timescale is varied via the mixture stoichiometry ($0.20 \leq \Phi \leq 1.0$) with the turbulence ($Re_t \simeq 361 \pm 12$) and counterflowing hot combustion products ($T_{HCP} = 1700$ K) kept constant. The mixing layer case with $\Phi = 0.0$ is also investigated. The choice of DME and EtOH is based on their relevance as alternative automotive fuels [26, 27], similar laminar flame properties and significantly different auto-ignition characteristics [28] with their relatively well established chemistries [29] an advantage. The methane flames provide a reference point. The impact of the fuel reactivity is investigated via a multi-fluid description [17] by means of simultaneous Mie scattering, hydroxyl – planar laser induced fluorescence (OH–PLIF) and particle image velocimetry (PIV). The analysis extends bimodal descriptions [30] by including a wider range of fluid states (i.e. reactants, products, mixing, weakly and strongly reacting fluids) and has been found particularly useful when delineating low Da combustion [16, 17, 31]. The study further provides information on the conditions leading to burning mode transitions via (i) multi-fluid probabilities, (ii) structural flow field information and turbulence-flame interactions delineated by means of conditional (iii) velocity statistics and (iv) the rate of strain along fluid iso-contours. (v) A Da based analysis is performed to delineate conventional and auto–ignition combustion modes.

2. Experimental Configuration

The current back–to–burnt (BTB) opposed jet configuration has distinct advantages for the systematic investigation of burning mode transitions from flamelet-like structures towards distributed reaction zones. These include (i) relatively well developed turbulence [32, 33]; (ii) separate control of chemical and turbulent timescales [34]; (iii) flame stabilisation related to the intrinsic aerothermochemistry [16, 17, 37]; and (iv) a well controlled burnt gas state can be used to stabilise flames beyond conventional extinction points [17].

2.1. Burner Configuration

The original opposed jet facility was developed by Geyer et al. [36]. Geipel et al. [32] introduced cross fractal grids (CFGs) and Goh et al. [14, 15, 35] optimised the nozzle geometry to remove low frequency jet instabilities [32, 38]. The use of CFGs [32] induces a turbulent flow field with a multi-scale character [37] and realises a high turbulence to bulk strain ratio while eliminating bulk flow instabilities [35]. The current optimal burner (see supplementary material) is identical to that used by Hampp et al. [16, 17, 39] with the nozzle separation (H) set to one nozzle diameter ($D = 30$ mm).

Two separate gas mixing systems provide the reactants, i.e. dried and filtered Howden air, DME (99.9%), CH_4 (99.9%), H_2 (99%) and CO_2 (99%). The gas flow rates are supplied with an uncertainty $< 0.8\%$ at full scale [32] and prevapourised ethanol is supplied using the liquid fuel system [14]. Co-flow velocities are set to 30% of the upper nozzle (UN) bulk velocity [32].

2.2. Flow Conditions

The premixed fuel / air mixtures are injected through the upper nozzle and stabilised against hot combustion products (HCP) emerging from the

Table 1: Experimental Conditions. FBA – Flash Back Arrestor, FSM – Flame Stabilising Mesh; Dil. – Dilution; NL – Nozzle Length; Cross Fractal Grid (CFG) [16].

UN Conditions Unburnt Reactants		LN Conditions Hot Combustion Products	
$\dot{V}_{UN}$	7.07×10^{-3} m^3 s^{-1} (293 K)	$\dot{V}_{LN}$	3.10×10^{-3} m^3 s^{-1} (293 K)
$U_{b,UN}$	11.2 m s^{-1} (320 K)	$U_{b,LN}$	24.0 m s^{-1} (1700 K)
Fuel	DME, EtOH, CH_4	Fuel	H_2
Φ_{UN}	0.0 – 1.0	Φ_{LN}	1.0
T_r	320 K	T_{HCP}	1700 K
Grid	CFG	Grid	FBA and FSM
NL	50 mm	NL	100 mm
Re	$\sim$ 19,550	Dil.	22% by volume of CO_2
Re_t	$\sim$ 361		

lower nozzle. The flow conditions are listed in Table 1.

2.2.1. Upper Nozzle Conditions

The CFG is installed 50 mm upstream of the UN exit providing a relatively well developed turbulent flow field [32]. The equivalence ratio of the premixed fuel / air mixtures is varied from $0.20 \leq \Phi \leq 1.0$ with the mixing layer ($\Phi = 0.0$) also investigated. The reactants are injected with a constant bulk velocity of $U_b = 11.2$ m s^{-1} leading to bulk and turbulent strain rates of $a_b = 2 \cdot U_b/H \simeq 750$ s^{-1} and $a_T \geq 3200$ s^{-1}, respectively [17]. In order to avoid re-condensation of ethanol, reactants are preheated to $T_r = 320$ K to raise the vapour pressure well above the maximum fuel mole fraction. The current flow conditions realise a constant $Re_t \simeq 361 \pm 12$ determined based on the integral length scale of turbulence ($L_I = 3.9 \pm 0.2$ mm) and velocity fluctuations ($u_{rms} \simeq 1.6$ m s^{-1}) measured using hot wire anemometry at the UN exit [19]. The u_{rms} is within 10% of that measured with PIV at 1 mm from the UN nozzle exit (for locally axisymmetric turbulence $u_{rms} = 1/3(u' + 2 \cdot v')$, where u' and v' are the axial and radial fluctuations).

2.2.2. Lower Nozzle Conditions

The lower nozzle burnt gas state is obtained using premixed stoichiometric H_2/air flames diluted with 22% CO_2 by volume prior to combustion to control the temperature. The flames are stabilised on a mesh that is installed 100 mm upstream of the nozzle exit [16]. The nozzle exit temperature is set to $T_{HCP} = 1700 \pm 3.5$ K, measured via a 50 μm type R thermocouple. The stagnation plane is located in the proximity of the burner centre by matching jet nozzle momenta via a burnt gas velocity of 24 m s^{-1}. The residence time ($\sim$ 6 ms) of the burnt gases in the lower nozzle provides hot combustion products in close–to chemical equilibrium with major species concentrations accounting for $> 99.8\%$ of the total ($[N_2] = 3.63$, $[H_2O] = 1.91$, $[CO_2] = 1.56$, $[CO] = 4.38\times10^{-2}$ $[O_2] = 2.85\times10^{-2}$, $[H_2] = 1.55\times10^{-2}$ mol m^{-3}). The constant thermochemical state provides a constant $[OH]^{\ddagger} \approx 8.82\times10^{-3}$ mol m^{-3} and a clearly detectable fluorescence intensity ($I^{\ddagger}$) with a signal to noise ratio (SNR) = 3.5 [17]. The measured $I^{\ddagger}$ and computed $[OH]^{\ddagger}$ provide the reference values used to calibrate the OH intensity segregation technique [17].

2.3. Measurement Setup, PIV and Image Preparation

The diagnostic setup, summarised below, has been discussed by Hampp and Lindstedt [17] including comprehensive uncertainty and error analyses. Simultaneous Mie scattering, PIV and OH-PLIF measurements are conducted. Two light sheets (532 nm and 281.7 nm) with a height of 1D and thickness < 0.25 mm and < 0.50 mm, respectively, are superimposed. Mie scattering is recorded using a LaVision ProX 4M camera (2×2 binning) equipped with a Tokina AF 100 mm lens (f/2.8) and narrow bandpass filter (3 nm centred at 532 nm). A dichroic beam splitter is used to spectrally separate the OH fluorescence signal from the Mie scattering. OH-PLIF is

recorded via a LaVision Imager Intense camera connected to an intensified relay optics (LaVision IRO) unit that is equipped with a 105 mm ultraviolet lens (f/2.8). A bandpass filter with a transmissivity $> 85\%$ from 300 – 320 nm and an optical density > 5 to block the laser lines is used. A temporal separation of 25 μs between the PIV laser pulses is found ideal to minimise spurious vectors. The OH-PLIF images are obtained from the first pulse. Aluminium oxide powder ($d_{p,50} = 0.44$ μm and $d_{p,90} = 1.7$ μm) is used as a velocity tracer with both nozzles seeded separately. Cross-correlation PIV with decreasing interrogation region size (128 $\times$ 128 to 48 $\times$ 48 with a 75% overlap) is applied using LaVision Davis 8.1. A high accuracy mode with adaptive interrogation window shape modulation is used for the final pass [40]. The velocity field is resolved by 115 $\times$ 88 vectors, providing a spacing of 0.30 mm and spatial resolution of $\lambda_{PIV} = 0.60$ mm [17]. A control PIV calculation with $\lambda_{PIV} = 0.30$ mm (i.e. 24 $\times$ 24, 50% overlap) showed differences in the velocity statistics $< 0.5\%$. This suggests a modest impact of the spatial resolution on conditioning based on fields in close proximity. A minimum of 3000 realisations per condition are recorded to achieve statistical independence. Pre-processing steps of the recorded images (i.e. alignment, data reduction, noise reduction, shot-to-shot intensity fluctuations and white image correction) were described by Hampp et al. [17, 39].

3. Chemical Timescales and Limiting Conditions

The current experimental conditions provide both thermally supported and self-sustained flames [16, 17]. Self-sustained flames at high Da flames detach from the stagnation plane and anchor in low strain regions. With reducing Da, the strain acting on the flame surface increasingly results in

local extinction, with global extinction prevented by the turbulent transport of HCP fluid across the stagnation plane [14, 16, 41]. Chemical timescales and laminar flame properties are determined computationally to support the analysis of experimental data in terms of non-dimensional groups (e.g. Da numbers). The latter are determined based on the properties at the upper nozzle exit to provide an indication of the expected regime of turbulence–chemistry interactions, e.g. Da, and degree of local extinction. The reaction mechanism of Park [29] is used in combination with the hydrogen chemistry of Burke et al. [42]. The mechanism was validated against laminar burning velocities [43–45] and species profiles [46, 47] by Park [29] and auto-ignition delay times (τ_{ai}) by Hampp [39] with good agreement. The calculations are further validated here for flame extinction using experimental data from Wang [25] for DME and EtOH and Law et al. [48] for CH_4 with satisfactory agreement as shown in the supplementary material.

3.1. Strained Laminar Flame Extinction Points

Self-sustained high Da flames in the BTB configuration decouple from the hot combustion products provided by the opposing (lower nozzle) jet and conventional aerothermochemistry criteria apply. A minimum (critical) integrated heat release rate ($\int \dot{Q}_q$) is required for self-sustained flame propagation [17]. Values of $\int \dot{Q} < \int \dot{Q}_q$ lead to the extinction of conventional flames in both the twin flame and back-to-burnt configuration. The thermochemical state (e.g. peak temperature and peak species concentrations) is well correlated with $\int \dot{Q}$ and segregate self-sustained from thermally supported burning in BTB flames. Well resolved (i.e. > 25 cells across the CH peak) strained laminar counterflow calculations [49] provide the chemical timescales and flame properties as a function of equivalence ratio and fuel

Table 2: Twin flame extinction point conditions for premixed fuel/air twin flames.

Fuel		DME		EtOH		CH_4	
Φ	–	0.60	1.0	0.60	1.0	0.60	1.0
a_q	s^{-1}	575	3000	400	2400	550	1900
T_q	K	1515	1759	1495	1751	1531	1837
$[OH]_q/[OH]^{\ddagger}$	–	3.5	5.8	3.0	5.4	3.2	4.5
$\int \dot{Q}_q$	MW m^{-2}	0.23	0.75	0.18	0.68	0.22	0.62

type. The extinction strain (a_q) and peak OH concentration at extinction $[OH]_q$ are determined in a twin flame configuration with results summarised in Table 2 along with the peak temperature at extinction (T_q) and $\int \dot{Q}_q$. At $\Phi = 0.20$ the extinction strain is significantly lower than the bulk strain and corresponding cases are excluded. The laminar burning velocity (S_L) and laminar flame thickness (δ_f, i.e. the 5 – 95% fuel consumption layer [50]) are determined using a BTB configuration (corresponding to the experiment) with results summarised in Table 3. As the Da is reduced, combustion is increasingly supported by the hot combustion products.

3.2. Flame Parameters and Dimensionless Groups

The Re_t is maintained constant in the current study, while the Damköhler and Karlovitz numbers, see Eq. (1), are varied by means of the chemical timescale (τ_c) through the equivalence ratio and fuel type.

$$Da = \frac{\tau_I}{\tau_c} \; ; \qquad Ka^{-1} = \frac{\tau_\eta}{\tau_c} \tag{1}$$

The integral timescale of turbulence (τ_I) is based on the measured u_{rms} = 1.6 m s^{-1} and L_I = 3.9 mm, while the chemical timescale is obtained from the calculations as defined in Eq. (2). Kolmogorov timescales ($\tau_\eta \simeq$ 135 μs) and length scales ($L_\eta = \nu_r^{3/4} \cdot \varepsilon_r^{-1/4} \simeq$ 48 μm) are based on the

rate of dissipation ($\varepsilon_r = u_{rms}^3 \cdot L_I^{-1}$) and the kinematic viscosity (ν_r) in the reactants, see Table 3.

$$\tau_I = \frac{L_I}{u_{rms}}; \qquad \tau_c = \frac{\delta_f}{S_L}\ ; \qquad \tau_\eta = \sqrt{\frac{\nu_r}{\varepsilon_r}} \tag{2}$$

The resulting ranges of Damköhler numbers and Karlovitz numbers are $6.0{\cdot}10^{-2} \leq Da \leq 5.1$ and $3.3{\cdot}10^{-3} \leq Ka^{-1} \leq 0.27$, respectively. The Taylor microscale and Reynolds number follow from $L_\lambda = 10^{1/2} \cdot L_\eta^{3/4} \cdot L_I^{1/3}$ and $Re_\lambda = L_\lambda \cdot u' \cdot \nu_r^{-1}$, respectively, with values listed in Table 3. Conventional regime diagrams, see Fig. 1, provide an estimate of the expected burning modes. The conditions cover the range $3.2 \leq u_{rms}/S_L \leq 40$ with the intense turbulence regime limit $u_{rms}/S_L \simeq 19$ [51].

The mean turbulent strain exceeds the laminar extinction strain for all cases (see Table 2). This suggests that HCP support, which can cause auto-ignition, is required to sustain combustion beyond the conventional (strained twin flame) extinction limit. The ignition delay times (τ_{ai}) and the resulting auto–ignition based $Da_{ai} = \tau_I \cdot \tau_{ai}^{-1}$, evaluated at initial temperatures of 1300, 1500 and 1700 K, are plotted in Fig. 2 and listed in Table 3. The temperature range approximately covers the onset of high temperature chain-branching up to that of the HCP. The trend of the auto-ignition delay times for DME and EtOH (i.e. shorter τ_{ai} for DME compared to EtOH at low and intermediate initial temperature and vice versa at higher temperatures) was also observed by Tingas et al. [52, 53]. While approximate, the data suggests that Da_{ai} is larger than the flame based Da for temperatures above 1500 K and that conventional (e.g. flamelet-based) combustion can be (partially) expected for $\Phi \geq 0.60$ for DME and $\Phi \simeq 1.0$ for methane. The crossing of the Da and Ka^{-1} lines with the Da_{ai} symbols indicate the presence of a

burning mode related to auto-ignition within the most energetic and smallest turbulence scales, respectively. A strong fuel dependency is also evident in the burning mode transition. The fuel reactivity is directly related to, and fully consistent with, the corresponding cetane number for DME or RON / MON numbers of EtOH and CH_4 as well as the spontaneous auto-ignition temperatures. DME is a diesel-like fuel with a high cetane number of 55 – 60 [54], while EtOH and methane exhibit high octane numbers, i.e. RON / MON of 110 / 90 [55] and > 120 [56], respectively. Spontaneous auto-ignition temperatures vary significantly at 508 [57], 642 [58], 868 K [59] for DME, EtOH and CH_4, respectively.

4. Multi–Fluid Post–Processing

Turbulence – chemistry interactions in low Da flows cannot be quantified by bimodal (i.e. reactants and products) descriptions as intermediate states become statistically significant [5]. Furthermore, auto–ignition based combustion may become significant or dominant. Therefore we recently adopted a multi-fluid description that incorporates a wider range (e.g. mixing, weakly and strongly reacting fluids) of states [16, 17]. The methodology, briefly outlined below, was found instrumental for low Da flows and is here used to quantify fuel chemistry effects on burning mode transitions.

The current multi-fluid analysis uses a conventional PIV tracer particle based density segregation technique, e.g. [37, 60, 61], in combination with a threshold based OH intensity band classification. The first threshold is based on experimental observations and the second on well established combustion theories (see below). For the conditions of interest, i.e. fuel lean combustion and the presence of OH in regions with $T \geq 1200$ K, a linear relation

Table 3: Summary of turbulent and chemical conditions to derive the turbulent Reynolds, Damköhler and Karlovitz numbers for DME, EtOH and CH_4 at varying Φ and low strain rate (a = 75 s^{-1}). Sc is the Schmidt number and $\overline{U_{r,NE}}$ is the mean axial reactant velocity 1 mm away from the UN exit. The reactant temperature was T_r = 320 K and the turbulence conditions were evaluated within the reactants.

Fuel	–	DME			EtOH			CH_4				Air
Φ	–	0.20	0.60	1.0	0.20	0.60	1.0	0.20	0.60	0.80	1.0	0.0
S_L	m s^{-1}	0.04	0.21	0.50	0.04	0.17	0.46	0.04	0.15	0.36	0.39	–
δ_f	mm	1.3	0.46	0.24	1.4	0.55	0.26	1.7	0.85	0.49	0.44	–
T_{ad}/T_r	–	2.8	5.5	7.2	2.8	5.5	7.2	2.7	5.3	6.3	7.0	–
τ_c	ms	33	2.2	0.48	36	2.9	0.57	41	5.7	1.6	1.1	–
$\tau_{ai,1700}$	μs	61 ± 7.0			60 ± 1.8			196	219	231	242	–
$\tau_{ai,1500}$	μs	173 ± 9.0			264 ± 5.4			832	1053	1128	1194	–
$\tau_{ai,1300}$	ms	1.62	1.11	0.93	3.1	2.7	2.5	11.3	15.2	16.2	17.0	–
$\nu_r \times 10^6$	m^2 s^{-1}	17.5	17.0	16.5	17.5	17.0	16.5	17.8	17.9	18.0	18.0	17.9
Sc	–	0.72	0.73	0.73	0.72	0.73	0.73	0.74	0.76	0.77	0.78	0.72
u'	m s^{-1}	1.7	1.8	1.8	1.7	1.6	1.9	1.9	1.9	2.0	2.0	1.7
$\overline{U_{r,NE}}$	m s^{-1}	9.4	9.5	10	10	9.7	10	9.4	9.4	10	9.2	10
u_{rms}	m s^{-1}				1.6 ± 0.1							
L_I	mm				3.9 ± 0.2							
τ_I	ms				2.4							
L_λ	μm				287 ± 4							
L_η	μm				48							
τ_η	μs				135 ± 2							
$\overline{u^*}/u'$	–	2.7	2.9	3.4	2.7	2.7	3.0	2.7	2.7	2.7	2.7	2.7
δ_l/L_I	–	0.42	0.86	1.0	0.17	0.50	0.93	0.23	0.33	0.70	0.52	0.23
Re_t	–	357	367	378	356	367	378	351	349	347	347	349
Re_λ	–	28	30	31	28	27	33	31	30	32	32	27
Da	–	0.08	1.2	5.1	0.08	1.0	4.4	0.06	0.44	1.5	2.1	–
$Da_{ai,1700}$	–	40 ± 4.6			40 ± 1.2			12	11	10	10	–
$Da_{ai,1500}$	–	14 ± 0.7			9.1 ± 0.2			2.9	2.3	2.1	2.0	–
$Da_{ai,1300}$	–	1.5	2.2	2.6	0.77	0.88	0.97	0.21	0.16	0.15	0.14	–
$Ka^{-1} \times 10^3$	–	4.1	61	281	3.8	47	237	3.3	24	84	123	–

is sufficient (uncertainty $< 10\%$) to link relative theoretical OH concentrations to the experimentally observed fluorescence intensity and to identify characteristic intensity bands [17, 39, 62]. The fluids states are:

Reactants: Fresh reactants emerging from the UN that have not undergone any thermal alteration (i.e. no oxidation or mixing processes). The

reactants are detected via a conventional PIV tracer particle based density segregation technique, e.g. [37, 60, 61], capable of detecting multiple and fragmented splines.

Mixing fluid: A fluid state that has been exposed to a thermal change prior the onset of OH producing chemical reactions (e.g. via mixing with HCP). The mixing fluid is detected by the superimposition of the Mie scattering and OH-PLIF images and is identified in regions with low seeding density and no OH signal.

Strongly reacting fluid: Regions with a high OH signal intensity consistent with self-sustained (e.g. flamelet) burning (see Sec. 4.1). Conventional extinction criteria apply [41, 63].

Weakly reacting fluid: A fluid state with modest levels of OH, e.g. ultra lean flames sustained by support from an external enthalpy source and/or combustion products approaching equilibrium (see Sec. 4.1).

Hot combustion products: The HCP emerge from the lower nozzle in close–to chemical equilibrium at 1700 K and provide a well defined reference state with a constant $[\mathrm{OH}]^{\ddagger}$ (see Sec. 3.1) and signal intensity ($I^{\ddagger}$) that is used to calibrate the OH band segregation. The maximum measured OH signal of the mixing layer case ($\Phi = 0.0$) is used to separate the HCP from fluid elements containing OH originating from combustion with $\Phi > 0$. The limiting threshold $\Lambda_p = \lceil I/I^{\ddagger} \rceil = 2.0$ is independent of the UN conditions (i.e. Φ, fuel type). The excess ($1.0 < I/I^{\ddagger} < 2.0$) stems from oxidation of residual reactants in the HCP.

The density segregation technique, the delineation of the mixing fluid and the definition of the product fluid threshold (Λ_p) are identical to Hampp and

Lindstedt [17] and based on experimental observations. The segregation of the weakly and strongly reacting fluids is extended, as outlined below, to accommodate the different fuels.

4.1. OH Containing Fluid States

The thermochemical state at the twin flame extinction point (e.g. $[\mathrm{OH}]_q$ see Table 2) segregates self-sustained from thermally supported burning in the current BTB configuration [17]. Regions with an OH fluorescence intensity ratio beyond the non-dimensional (extinction) threshold (see Table 2) defined by Eq. (3) are consequently assigned to the strongly reacting fluid (i.e. self-sustained burning).

$$\Lambda_{q(\Phi)} = \frac{[\mathrm{OH}]_{q(\Phi)}}{[\mathrm{OH}]^{\ddagger}} = \frac{I_{q(\Phi)}}{I^{\ddagger}} \qquad \forall \text{ fuels and } \Phi \geq 0.60 \tag{3}$$

The weakly reacting fluid (e.g. thermally supported burning) follows as $\Lambda_p < I/I^{\ddagger} < \Lambda_q$ and can originate from (i) ignition events, (ii) decaying OH concentration in combustion products or (iii) chemically active material that is diluted by the HCP.

4.2. Multi-Fluid Fields and Velocity Conditioning

Superposition of the segregated Mie scattering image (i.e. reactants and thermally altered fluid material) and the three intensity bands of the OH – PLIF image (i.e. hot combustion products, weakly and strongly reacting) yield a quinary multi-fluid image as exemplified in Fig. 3. The spatial resolution of the multi-fluid analysis was determined based on the smallest resolved line pair of a post-processed image (i.e. same spatial filters and denoising functions) of a 1951 USAF target to $\lambda_{MF} \simeq 250$ μm, i.e. L_I / $\lambda_{MF} \simeq 16$ [17]. The mean scalar dissipation layer thickness ($\lambda_D =$

$11.2 \cdot L_I \, Re_t^{-3/4} \, Sc^{-1/2}$) [64] is resolved ($\lambda_D \, / \, \lambda_{MF} \simeq 2.5$), while the Batchelor scale ($\lambda_B = L_\eta Sc^{-1/2}$) [65] is under-resolved ($\lambda_B \, / \, \lambda_{MF} \simeq 0.22$). Values for the Schmidt number (Sc) are listed in Table 3. The multi-fluid probabilities were compiled from the statistics of the prevalence of a given fluid state at a particular physical location. Multi-fluid velocity conditioning (see Eq. (4)) is used to extend the analysis based on bimodal statistics [35, 37, 60, 61, 66].

$$
\begin{aligned}
\overline{U}_{k,FS,i,j} &= \frac{1}{N} \sum_{n=1}^{N} c_{FS,n,i,j} \cdot U_{k,n,i,j} \quad \forall \; i,j \\
(u'u')_{k,FS,i,j} &= \frac{1}{N} \sum_{n=1}^{N} c_{FS,n,i,j} \cdot \left(U_{k,n,i,j} - \overline{U}_{k,FS,i,j} \right)^2 \quad \forall \; i,j \\
C_{FS,i,j} &= \frac{1}{N} \sum_{n=1}^{N} c_{FS,n,i,j} \quad \forall \; i,j \\
\textstyle\sum_{FS} C_{FS} &\coloneqq 1
\end{aligned}
\tag{4}
$$

In Eq. (4), $c_{FS,n}$ is the instantaneous conditioning variable, i.e. unity within the fluid state (FS) and nil outside, k the velocity component, n the instantaneous image, N the number of images (3000) with i and j indices.

5. Results and Discussion

The multi-fluid probability and conditional velocity statistics are aligned at the first iso-contour (i.e. $x_s = 0$) where a temperature change is detected by the density segregation technique (see Fig. 3) to eliminate the movement and rotation (within an envelope defined by L_I) of the stagnation plane [35]. The multi-fluid probabilities (Sec. 5.2), interface (Sec. 5.3) and conditional velocity statistics (Sec. 5.4) are evaluated along the theoretical stagnation point streamline (SPS), i.e. $y = 0$ in Fig. 3. The strain analysis in Sec. 5.6 is conditioned on $y = 0 \pm 1/2 \; L_I$ to include the radial movement of the

stagnation point [32].

5.1. Detached and Self-Sustaining Flames

The leading edge of the $\overline{c}$ scalar field (i.e. $\overline{c} = 0.02$ iso-contour) is determined from the statistics of the location of the instantaneous reaction onset. Thus, for self-sustained flames $\overline{u^*} = \overline{u}|_{\overline{c}=0.02}$ [67] defines the corresponding turbulent burning velocity. However, for thermally supported low Da flames $\overline{u^*}$ corresponds to the velocity at the leading edge of the mixing layer. The $\Phi = 0.0$ case provides the reference for pure mixing in the absence of heat release and is located at $\overline{u^*}/u' = 2.7$. For the current conditions, the HCP influence becomes reduced for DME flames with $\Phi \geq 0.60$ and for stoichiometric EtOH flames as shown in row of values of $\overline{u^*}/u'$ listed in Table 3. By contrast, for methane the HCP influence remains dominant for all Φ. The above definition [67] can also be used to determine unique (not influenced by HCP support) turbulent burning velocities in the twin flame opposed geometry.

The gradual detachment of the flame from the stagnation plane is illustrated by the thickness of the layer δ_l defined as the distance between the axial position of the leading edge of $\overline{c}$ and the leading edge of the stagnation plane. The latter is determined from the statistics of the location of the HCP iso-contour. The mixing layer for the $\Phi = 0.0$ case has a thickness $\delta_l/L_I = 0.23$. With increasing Φ (i.e. Da) the leading edge of $\overline{c}$ shifts away from the stagnation plane. For DME, δ_l/L_I increases from 0.42 to 1.0 for $\Phi = 0.20$ to 1.0, respectively. By contrast, the EtOH (CH_4) cases show an attenuated detachment of $\delta_l/L_I = 0.17$ (0.23) and 0.93 (0.52) for $\Phi = 0.20$ and 1.0, respectively. All values are listed in Table 3.

5.2. Multi-Fluid Probability Statistics

The reactant fluid probability, conditioned on the SPS and aligned at $x_s = 0$, is found to be fuel and equivalence ratio independent and are hence omitted as the DME case has been discussed by Hampp and Lindstedt [17]. By contrast, the mixing fluid probability ($P(m)$) has distinct fuel type and Φ related differences as shown in the top row of Fig. 4. The peak probability for low Da flames (i.e. $\Phi \leq 0.60$) is broadly constant for a given fuel at 0.96 for DME, 0.81 for CH_4 and 0.64 for EtOH. The reduced value for EtOH is repeatable [39] and discussed below. The residual percentiles at $x_s = 0$ exhibit a low OH signal intensity consistent with the HCP fluid state. Mixing layers below the multi-fluid resolution are not considered. The DME mixing fluid peak probability and its spatial extent reduces significantly with increasing Da (i.e. $\Phi = 1.0$) as chemical active fluid states are favoured. The EtOH mixing fluid shows the same trend, but with an attenuated reduction in $P(m)$ with increasing Da. By contrast, the need for thermal support for the CH_4 flames remains with a peak mixing fluid probability $\sim$70% for the stoichiometric case. This is consistent with the iso–contour based analysis relating to self–sustained flames presented in Sec. 5.1.

The weakly reacting fluid probability ($P(w)$) is shown in the middle row of Fig. 4 for all fuels. DME and EtOH show similar distributions with peak values increasing from around 10 to 38% with an increase of Φ from 0.20 to 0.60. The shape and spatial variation of $P(w)$ for CH_4 differ substantially from the oxygenated fuels, yet the increase in peak value is approximately maintained (5 – 26%). DME and EtOH show a much stronger decay compared to CH_4 as indicated by the probability tails. The phenomena was repeatable [31] and was qualitatively also observed by Shen and Sutton [68]. For $Da > 1.0$, the peak of $P(w)$ reduces in favour of a gradual transition to

the strongly reacting fluid – particular evident for the stoichiometric DME case. The weakly reacting fluid probability is only modestly reduced for EtOH and CH_4 indicating the distinct need of thermal support to initiate and sustain chemical activity under current turbulence conditions.

The strongly reacting fluid probabilities $P(s)$ are depicted in the bottom row of Fig. 4. At $Da \ll 1$ (i.e. $\Phi = 0.20$) self–sustained combustion is not observed. With Da of $\mathcal{O}(1)$ at $\Phi = 0.60$ peak probabilities of $P(s) \leq 20\%$ are obtained. The stoichiometric flames show a substantial increase in the strongly reacting fluid for DME and EtOH and a modest increase for CH_4, realising peak probabilities of 72, 47 and 20%, respectively. The trend is consistent with the determined laminar flame extinction points listed in Table 2. In the absence of conventional flame propagation, DME is the most likely fuel to support a transition to an auto-ignition related burning mode due to the higher Da_{ai} at modest temperatures, see Fig. 2 and Table 3.

5.3. Multi-Fluid Interface Statistics

The multi-fluid delineation also supports a statistical analysis of interfaces between adjacent fluid states along the theoretical stagnation point streamline. In combination with PIV and streamline calculations, three flow scenarios were defined: (i) the streamline tangent ($\hat{\mathbf{s}}$:= positive in flow direction) and interface normal ($\hat{\mathbf{n}}$:= positive from reactants to HCP) are aligned, i.e. $\hat{\mathbf{s}} \cdot \hat{\mathbf{n}} > 0.31$, (ii) the opposite with $\hat{\mathbf{s}} \cdot \hat{\mathbf{n}} < -0.31$ and (iii) tangential flow, i.e. $||\hat{\mathbf{s}} \cdot \hat{\mathbf{n}}|| < 0.31$ (i.e. 72 – 108°). The three cases correspond to transport (i) into a fluid state, (ii) out of it and (iii) sheared or aligned flow of two fluid states. The methodology was described in detail by Hampp and Lindstedt [17] and a schematic is provided in the supplementary material.

Cases with probabilities $> 1\%$ are shown in Fig. 5. The line weight

indicates the likelihood of adjacent fluid state pairs, the arrows indicate the three flow scenarios, the numbers show the likelihood of the corresponding flow scenarios in percent based on the total number of interfaces and the dashed lines show insignificant flow paths. Single-headed arrows point in the flow direction and the double-headed arrow indicates tangential flow. The numbers in Fig. 5 are normalised using all interfaces for each case. In the following we discuss (i) the cumulated interface probabilities of a flow path to quantify the reaction progress, (ii) the dominant flow directions to quantify turbulence – chemistry interactions and (iii) the statistical relevance of adjacent fluid state pairs normalised by the number of multi-fluid images. Consequently, the values in (iii) are larger when compared to (i) as every multi-fluid image contains multiple material transitions and thus interfaces.

For $Da < 1$ ($\Phi = 0.20$) the majority of the reactant fluid is adjacent to a mixing fluid layer, i.e. DME with 96%, EtOH with 73% and CH_4 with 88%, and HCP accounting for the residual percentiles. This agrees well with the corresponding peak mixing fluid probabilities adjacent to the origin x_s (see Fig. 3) in Sec. 5.2. The proportion of reactant to mixing fluid interfaces is 39, 31 and 40% for DME, EtOH and CH_4 (top row) with the corresponding HCP to mixing fluid interfaces responsible for 42, 34 and 44%.

The weakly reacting fluid at $Da < 1$ (i.e. $\Phi = 0.20$ for all fuels) is found almost exclusively ($> 90\%$) adjacent to the HCP fluid with cumulated interface probabilities of 17, 21 and 9% for DME, EtOH and CH_4. This is indicative of low OH gradients governed by turbulent mixing or thermal support layers. In general, the multi-fluid structure at $\Phi = 0.20$ is broadly fuel type independent, though a reduced probability of finding weakly reacting fluid adjacent to HCP can be noted for methane.

The higher reactivity of DME, compared to EtOH and CH_4, results in

some differences between the fuels for the $Da \simeq 1$ ($\Phi = 0.60$) cases in terms of how strongly reacting fluid may be separated from the reactants via thermal support layers (i.e. mixing or HCP fluid). However, the primary path for the weakly reacting fluid is fuel independent and similar to the lower Da ($\Phi = 0.20$) flames. Thus, the weakly reacting fluid is dominated by turbulent transport of HCP into the reactants. Secondary paths arise through the mixing fluid and for EtOH also directly from the reactants. This observation suggests rapid thermal decomposition of EtOH when in contact with HCP. The flame computations suggest that the reaction $C_2H_5OH \rightarrow C_2H_5 + OH$ accounts for 11.5±0.1 of the consumption of ethanol and the resulting [OH] is sufficient for the detection of the weakly reacting fluid state for all Φ.

For stoichiometric cases, the likelihood of detectable ($\lambda_{MF} = 250\ \mu m$) reactant adjacent to mixing fluid is reduced to ∼25% for DME and EtOH with an interface probability of ∼8%. By contrast, the corresponding fluid state pair probability remains > 80 % for CH_4 (i.e. 27% of all interfaces) illustrating the continuous need for thermal support. A strong augmentation of flamelet-like structures is evident for the stoichiometric DME flame. The probabilities of finding strongly reacting fluid directly adjacent to the reactant fluid are 57, 24 and 9% (corresponding to 16, 8 and 3% of all interfaces) for DME, EtOH and CH_4, respectively. The stoichiometric DME and EtOH flames with high Da detach from the stagnation plane and show a preferential flow direction, e.g. dominant flow path from reactants into strongly reacting fluid as depicted in Figs. 5g – 5h, consistent with a flamelet–like structure. By contrast, the flow across weakly reacting fluid interfaces is mixing dominated with no clear direction evident. The cumulative interface probability leading to strongly reacting fluid (i.e. sum of shared interfaces with all other fluid state) further illustrates the delayed transition towards

self-sustained burning of EtOH (34%), and in particular CH_4 (18%), as compared to DME (52%). This is consistent with the fuel reactivity (see Table 2) and Chen et al. [69] who showed reduced ignition delay and elevated strain resilience of DME compared to CH_4.

5.4. Conditional Velocity Statistics

The impact of fuel reactivity on the flow field is further analysed using conditional multi-fluid velocity statistics. The data are conditioned on the SPS and aligned at $x_s = 0$. The mean conditional velocities and turbulent fluctuations are normalised by the mean axial reactant fluid velocity at the nozzle exit ($\overline{U_{r,NE}}$), see Table 3. A minimum of 75 vectors is used for the statistical analysis with a maximum change of 10% in the fluctuations within the last 20% of the sample. The reactant exit velocity is defined as negative.

5.4.1. Conditional Reactant Fluid Velocity

The conditional mean axial reactant fluid velocities ($\overline{U_{0,r}}$ / $\overline{U_{r,NE}}$) are depicted, along with the axial ($\overline{u'_{0,r}}/\overline{U_{r,NE}}$) and radial ($\overline{v'_{0,r}}/\overline{U_{r,NE}}$) fluctuations in Fig. 6. No distinct differences are observed between the fuels for $Da \ll 1$. The impact of differences in the combustion chemistry become evident for the cases with $\Phi = 0.60$. The higher fuel reactivity of DME promotes an advanced reaction onset and flame detachment from the stagnation plane. The mean velocity at $x_s = 0$ (the location of reaction onset) is in line with the natural reactant flow direction with $\overline{U_{0,r}}/\overline{U_{r,NE}}$ = -0.06. By contrast, $\overline{U_{0,r}}/\overline{U_{r,NE}} \simeq 0.02$ for EtOH and CH_4 indicating a HCP dominated reaction onset. With increasing Da (i.e. $\Phi = 1.0$), the reaction onset shifts further upstream towards the UN with elevated $\overline{U_{0,r}}/\overline{U_{r,NE}}$ = -0.24, -0.20 and -0.11 for DME, EtOH and CH_4, respectively. The modest difference

between DME and EtOH is consistent with the increased strain resilience of DME and thus a reduced frequency of local extinction. The trends are also consistent with the normalised mean velocity ($\overline{u^*}/u'$) at the leading flame edge, shown in Table 3, with no fuel chemistry effect apparent for $Da \ll 1$ where $\overline{u^*} = 2.7$ as for the $\Phi = 0.0$ mixing layer. For the DME case at $\Phi = 0.60$ $\overline{u^*}/u'$ increases to 2.9, while the EtOH and CH_4 remain mixing dominated with 2.7. For the stoichiometric cases, a further increase to 3.4 and 3.0 was observed for DME and EtOH. However, the reaction progress of the CH_4 remains governed by the HCP. This is consistent with the Da and Da_{ai} analysis. For example, conventional flame propagation for the methane cases is unlikely (as indicated by the low Da) and the initial temperature must exceed 1500 K to realise auto-ignition related burning (see Table 3). By contrast, auto-ignition related burning of DME is feasible for $T \geq 1300$ K with EtOH an intermediate case. The axial and radial reactant fluid fluctuations are reduced with increasing Φ, consistent with the gradual detachment of the reaction onset from the stagnation plane discussed in Sec. 5.1.

Reactant fluid pockets are observed at $x_s > 0$ with a probability $\leq 7\%$ due to fragmentation or three dimensional effects. The probability is independent of the mixture reactivity and fuel type [17, 39]. However, significant differences in the preferential flow alignment of these pockets are observed. For the stoichiometric cases with $Da > 1$, the interlayer is highly exothermic (e.g. strongly reacting fluid as inferred from Sec. 5.3) and induces a distinct convective direction of the reactant fluid pocket aligned with the main reactant flow. For DME with $\Phi = 1.0$ this results in an acceleration of the pocket towards the stagnation plane as indicated by the increasingly negative $\overline{U_{0,r}}$ / $\overline{U_{r,NE}}$ from $0 < x_s/L_I < 0.5$, see top right panel of Fig. 6. It further causes an alignment of $\overline{U_{0,r}}$ / $\overline{U_{r,NE}}$ with the natural reactant flow direction

for DME with $\Phi \geq 0.60$ and for EtOH/CH_4 with $\Phi = 1.0$. By contrast, the interlayer for $Da < 1$ (i.e. $\Phi = 0.20$) is formed by the mixing fluid and is hence governed by turbulent mixing across the stagnation plane. Reactant fluid pockets that align with the reactant fluid flow exhibit significantly (> 50%) reduced axial and radial fluctuations.

5.4.2. Conditional Weakly Reacting Fluid Velocity

The conditional mean axial weakly reacting fluid velocities ($\overline{U_{0,w}}$ / $\overline{U_{r,NE}}$) and its axial ($\overline{u'_{0,w}}$ / $\overline{U_{r,NE}}$) and radial ($\overline{v'_{0,w}}$ / $\overline{U_{r,NE}}$) fluctuations are depicted in Fig. 7. For flames with $Da < 1$ (i.e. $\Phi = 0.20$), the $\overline{U_{0,w}}$ / $\overline{U_{r,NE}}$ are nearly identical for all fuels. The $\overline{U_{0,w}}$ / $\overline{U_{r,NE}}$ of DME at $\Phi = 0.60$ separate from the EtOH and CH_4 cases and is in line with the UN reactant flow at $x_s = 0$, i.e. negative values. Moreover, attenuated axial velocity fluctuations are evident that can be attributed to enhanced dilatation. The weakly reacting fluid velocity of the stoichiometric DME and EtOH cases coincide and show reduced fluctuations compared to CH_4. The delayed separation of the reaction onset from the stagnation plane, the continuous requirement for substantial HCP support and, consequently, the attenuated dilatation effect on the weakly reacting fluid for CH_4 mixtures illustrates a strong influence of the fuel reactivity. The pronounced lower temperature reactivity [70] of DME causes advanced dilatation that is readily apparent for $Da \simeq 1$ (i.e. $\Phi = 0.60$). The conditional mean mixing fluid velocity is similarly governed by the HCP momentum and independent of the fuel reactivity for $Da \leq 1$. At $Da > 1$, the stoichiometric DME and EtOH cases are in line with the UN reactant flow direction at $x_s = 0$, while CH_4 flames remain strongly affected by the HCP stream. The data is provided in the supplementary material.

5.4.3. Conditional Strongly Reacting Fluid Velocity

The interface statistics presented in Sec. 5.3 suggest that the strongly reacting fluid can result from small HCP blending fractions depending on the reactivity of the mixture. Self-sustained burning is not realised for any fuel with $\Phi = 0.20$. For $\Phi = 0.60$ the conditional strongly reacting fluid mean velocity ($\overline{U_{0,s}}$ / $\overline{U_{r,NE}}$) for DME ($Da = 1.2$) case is distinctly lower compared to EtOH ($Da = 1.0$) and CH_4 ($Da = 0.44$) as depicted in Fig. 8. For DME the value of $\overline{U_{0,s}}$ / $\overline{U_{r,NE}}$ is lower than the corresponding weakly reacting fluid velocity, while EtOH and CH_4 flames show no clear difference. The DME case further exhibits distinctly reduced (50%) axial velocity fluctuations. For the stoichiometric flames with $Da > 1$ the discrepancies between DME and EtOH vanish and similar values of $\overline{U_{0,s}}$ / $\overline{U_{r,NE}}$ are obtained due to increasingly self-sustained flames detaching from the stagnation plane. The finding is consistent with the similar heat release parameters $\tau = (T_{ad} - T_r)/T_r = 6.1$ versus 5.9 and conventional burning properties (e.g. $S_L = 0.50$ versus 0.46 m s^{-1}) for DME and EtOH at $\Phi = 1.0$, respectively.

However, the likelihood of self-sustained combustion differs for DME and EtOH as shown in Fig. 4. The slightly more negative $\overline{U_{0,s}}$ / $\overline{U_{r,NE}}$ for the stoichiometric DME flame can be explained by the differences in $\overline{u*}/u'$ and the interface statistics, where a significant proportion of the strongly reacting fluid shares an interface with the reactant fluid. In contrast to these two fuels, the CH_4 flames show a reduced detachment from the stagnation plane and are consequently subjected to a higher rate of strain (discussed below). The strongly reacting fluid velocity shows a reduced dilatation away from the origin (i.e. $x_s/L_I > 0.5$) and is increasingly influenced by the counter-flowing HCP stream. This leads to substantially increased axial and radial

fluctuations for CH_4.

5.5. Fuel Effects at Similar Damköhler Numbers

The DME flame with $\Phi = 0.60$ ($Da = 1.2$) and an additional CH_4 case featuring $\Phi = 0.80$ ($Da = 1.5$) provide a comparison of two flames with similar and close-to unity Damköhler numbers. However, the two cases feature distinctly different auto-ignition delay times (factor of ~ 6) with the minimum for fresh reactants in contact with the HCP at 1700 K determined to be 62 and 371 μs for DME and CH_4, respectively [39]. This ratio increases to ~ 15 at an initial temperature of 1300 K. Comparisons are shown in Figs. 9 and 10. Strong similarities in the multi-fluid probabilities and the multi-fluid conditional velocities are evident. The reactant, mixing and strongly reacting fluid probabilities show a mean deviation of $< 4\%$ in the range from $0 < x_s/L_I < 1.5$. The mean difference in the weakly reacting fluid probability is $\sim$10% and is consistent with the shorter auto-ignition delay of DME.

The mean conditional reactant fluid velocities agree well as shown in Fig. 10. By contrast, the lower (i.e. alignment with the UN reactant flow) mixing and weakly reacting fluid velocity for DME again indicates reduced HCP blending fractions consistent with the different Da_{ai} characteristics. The larger negative conditional strongly reacting fluid velocity at $x_s = 0$ and enhanced dilatation at $x_s > 0$ for the CH_4 flame is consistent with the higher heat release of the closer to stoichiometric flame.

5.6. Conditional Strain Distribution on Material Surfaces

The rate of strain and vorticity are calculated from the instantaneous PIV data via Eq. (5). Conditioning on the multi-fluid material surfaces (β)

quantifies the actual rate of strain acting on the reaction zone and augments the estimated turbulent strain at the nozzle exit.

$$e_{ij} = \frac{1}{2}\frac{\partial u_i}{\partial x_j} + \frac{\partial u_j}{\partial x_i} \qquad \omega_{ij} = \frac{\partial u_i}{\partial x_j} - \frac{\partial u_j}{\partial x_i} \qquad f = \mathbf{R} \cdot e \tag{5}$$

The strain rate tensor is rotated by Θ, where $\mathbf{R}$ is the rotation matrix and Θ is the angle between the iso-contour normal and the SPS. This defines the normal ($a_n = f_{11}$) and tangential ($a_t = f_{22}$) strain components that are further, along with the vorticity, conditioned on the fluid state material surfaces (β) [16]. In addition, the total rate of strain ($a_d|\beta = e_{\beta,11} + e_{\beta,22}$) is evaluated. The determined instantaneous planar rates of strain are - to some degree - underestimated due to 3D effects [16]. The analysis is conducted within $\pm\ L_I/2$ radially away from the SPS to include the movement of the stagnation point [32]. In the following, only mean values are discussed with the PDF shapes shown in Figs. 11 and 12 and the rms spread provided in the supplementary material.

5.6.1. Strain Distribution along the Reactant Fluid Surfaces

The normal strain evaluated along the reactant fluid iso-contour is depicted in Fig. 11. The mean normal compressive strain at $\Phi = 0.20$ is fuel independent with $a_n|R$ = -1500 $\pm$ 50 s^{-1} as the reaction onset is dominated by mixing with HCP. The fuel dependency becomes apparent as Φ and thus Da increases. The mean $a_n|R$ for DME reduces by 70% from -1550 to -480 s^{-1} for $0.08 < Da < 5.1$, as shown in the first row of Fig. 11. By contrast, the corresponding rate of strain for the methane cases ($0.06 < Da < 2.1$) reduces by 18% towards lower compressive strain, while $a_n|R$ for EtOH experiences an attenuation of 58% ($0.08 < Da < 4.4$). The reduction of $a_n|R$ is indicative of a gradual detachment of the $\overline{c} = 0.02$ iso-contour from the stagnation

plane with increasing Da as discussed in Sec. 5.1 in the context of the flame stabilisation point. At high Da, the iso-contour is anchored in regions with an increased axial velocity, but low compressive strain, which is characteristic for a reaction onset driven by self-sustained burning. The upstream shift of the reactant fluid material surface further results in reduced levels of extensive tangential strain and a strong attenuation in conditional vorticity levels of 50%. By contrast, the reactant fluid surfaces for the CH_4 cases show no clear spatial separation from the stagnation plane with high $a_n|R$. The reaction onset in the proximity of the stagnation plane further causes a modest increase ($< 10\%$) of $a_t|R$ and a modest reduction ($\sim$13%) $\omega|R$ with increasing Φ. The earlier transition of DME and EtOH to strongly dilating fluid states, compared to CH_4, is also reflected in the total rate strain. For $\Phi = 0.20$, $a_d|R$ = -760 $\pm$ 20 s^{-1} and is only modestly affected by the fuel reactivity. By contrast, the reactant fluid iso-contours for the stoichiometric DME and EtOH cases are situated in regions of extensive total rates of strain ($a_d|R \simeq 320$ and 190 s^{-1} respectively), while the corresponding CH_4 iso-contour is found in compressive strain regions with $a_d|R$ = -420 s^{-1}.

It can further be noticed that DME and EtOH show strong similarities, while CH_4 shows a broadened PDF that is attributed to a pulsating burning mode that was previously observed at reduced Re_t by Mastorakos et al. [71]. Moreover, while the DME and EtOH cases with $Da > 1$ (in particular $\Phi = 1.0$) show a clear reduction of a_n with increasing Φ (c.f. $\Phi = 0.0$), the CH_4 cases show strong similarities for all stoichiometries. The rates of strain conditioned upon the mixing fluid material surface show similar trends with values provided in the supplementary material.

5.6.2. Strain Distribution along Chemically Active Fluid Surfaces

The compressive normal strain conditioned on the weakly reacting fluid material surface ($a_n|W$) is relatively fuel and equivalence ratio independent at $Da \lesssim 1$ (i.e. $\Phi \leq 0.60$) with $a_n|W$ = -1260±70 s^{-1}. The corresponding PDFs and values are provided in the supplementary material. However, the corresponding total rate of strain shows an attenuated contracting strain with increasing Φ for all fuels due to increased heat release. The conditional vorticity levels are consistently similar to the values found in the proximity of the stagnation plane ($\omega|W$ = 2500±250 s^{-1}). The absence of clear fuel dependent trends suggest a strong HCP influence with the accompanying modest heat release at high dilution ratios. This is consistent with the findings of Chakraborty and Swaminathan [72] that showed a lack of flow alignment for low Da flows with reduced heat release.

The strongly reacting fluid iso-contour is situated in low compressive strain ($a_n|S$) regions, as depicted in Fig. 12, with $a_n|S$ approximately 16% and 38% lower than the corresponding strain acting on the weakly reacting fluid for all fuels Φ = 0.60 and 1.0, respectively. The modestly higher a_n for DME compared to EtOH (i.e. -700 s^{-1} versus -520 s^{-1}) at Φ = 1.0 is consistent with the increased resilience of DME to strain as indicated by the calculated laminar extinction strain of a_q = 3000 s^{-1} and 2400 s^{-1} for DME and EtOH at Φ = 1.0, respectively, and also shown by Wang et al. [24]. Self-sustained DME flames can accordingly exist in regions where EtOH flames are extinguished or rely on thermal support to a greater extent. This is accompanied by a reduced $a_n|W$ of the stoichiometric EtOH flame compared to DME. The CH_4 flame remains located in the proximity of the stagnation plane with a compressive strain of -860 s^{-1}. Overall, the mean $a_n|S$ reduce

by 30, 50 and 17% with increasing Φ for DME, EtOH and CH_4.

Extensive tangential rates of strain remain approximately constant at $a_t|S$ (670 $\pm$ 110 s^{-1}) for all cases as increases in dilatation are balanced by the detachment from the stagnation plane. A shift from contracting ($a_d|S$ = -400 s^{-1}) to dilating strain (175$\pm$5 s^{-1}) total strain is evident with increasing Φ for DME and EtOH. A distinct reduction ($\sim$ 80%) in $a_d|S$ is evident for CH_4. The PDF spread for $a_n|S$ and $a_t|S$ at Φ = 0.60 is within 5% of weakly reacting fluid for all fuels. By contrast, the spread for the stoichiometric cases is 15% lower than that of the weakly reacting fluid. The reduction is attributed to an iso-contour governed by conventional flame propagation rather than turbulent mixing. This is consistent with the vorticity ($\omega|S$) reduction of $\sim$ 15% and $\sim$ 30% compared to $\omega|W$ at Φ = 0.60 and 1.0, respectively. The less pronounced strain reduction for the CH_4 cases is caused by the delayed onset of self-sustained flame propagation.

6. Conclusions

The current study has investigated the impact of fuel chemistry on burning mode transitions in turbulent fuel lean to stoichiometric premixed dimethyl ether, ethanol and methane flames. An opposed jet back–to–burnt configuration with a constant burnt gas state and fractal grid generated multi-scale turbulence was combined with a multi–fluid analysis based on simultaneous Mie scattering, OH–PLIF and PIV. The Damköhler number was varied through the mixture stoichiometry ($0.20 \leq \Phi \leq 1.0$) and fuel type. Based on a conventional combustion regime diagram, the conditions covered a transition from distributed reaction zones to close-to the corrugated flamelet regime with $0.06 \leq Da \leq 5.1$.

Multi-fluid probabilities, conditioned on the reaction onset iso-contour, and interface statistics have been used to quantify the impact of combustion chemistry with a more rapid transition to chemically active fluid states and self-sustained burning evident for DME due to its lower auto-ignition temperature and higher resilience to strain. This caused combustion to be anchored in regions of higher reactant fluid velocities for Da numbers around unity. By contrast, the transition from supported to a self-sustained flame propagation was delayed for EtOH and distinctly so for CH_4. The greater strain resilience of DME led to a slightly higher compressive strain along the iso-contours of chemically active fluid material compared to EtOH, while the further reduced reactivity of methane resulted in burning close to the stagnation plane and hence in regions characterised by high strain and vorticity.

The multi-fluid probabilities show that the aligned extent of the reaction zone is typically less than two integral length scales of turbulence. Inside the reaction zone, the probability of finding intermediate fluid states (i.e. beyond bimodal statistics) was found to be strongly fuel and Da number dependent with values exceeding 90% at low Damköhler numbers. A distinct impact of the fuel reactivity and ease to ignition was also observed in the weakly reacting fluid velocities, characteristic of HCP supported burning, with an advanced reaction onset and stronger pronounced dilatation observed for DME. The corresponding EtOH cases showed attenuated dilatation and a delayed reaction onset. Both phenomena were much more distinct for CH_4 and can partly be attributed to delayed auto-ignition facilitating higher HCP dilution rates. A comparison at identical Lewis number for DME and EtOH, fuels with similar laminar flame burning properties, further highlights the importance of the overall combustion chemistry in turbulent reacting flows. The chemistry differences cause large changes in conditional velocity statistics

and the impact is hence not subtle. Consequently, the data are expected to be particularly valuable for the development of models applicable to combustion processes that transition to distributed modes under conditions where the reaction progress can be controlled by an enthalpy source.

Acknowledgements

The authors would like to thank Dr Chiping Li, Dr Russ Cummings and Dr Douglas Smith and acknowledge the support of the AFOSR and EOARD under Grant FA9550-17-1-0021. The US Government is authorised to reproduce and distribute reprints for Governmental purpose notwithstanding any copyright notation thereon. The authors would also like to thank Dr Robert Barlow.

References

[1] T. Plessing, N. Peters, J. G. Wünning, Laseroptical investigation of highly preheated combustion with strong exhaust gas recirculation, Proc. Combust. Inst. 27 (1998), 3197–3204.

[2] F. J. Weinberg, Combustion temperatures: The future?, Nature 233 (1971), 239–241.

[3] V. D. Milosavljevic, R. P. Lindstedt, M. D. Cornwell, E. J. Gutmark, E. M. Váos, Combustion Instabilities Near the Lean Extinction Limit, in G. Roy, K. H. Yu, J. H. Whitelaw, J. J. Witton (Eds.), Advances in Combustion and Noise Control, Cranfield University Press, 2006, 149–165.

[4] J. A. Wünning, J. G. Wünning, Flameless oxidation to reduce thermal NO-formation, Prog. Energ. Combust. 23 (1997), 81–94.

[5] Y. Minamoto, N. Swaminathan, R. S. Cant, T. Leung, Reaction Zones and Their Structure in MILD Combustion, Combust. Sci. Technol. 186 (2014), 1075–1096.

[6] B. Savard, G. Blanquart, Effects of dissipation rate and diffusion rate of the progress variable on local fuel burning rate in premixed turbulent flames, Combust. Flame 180 (2017), 77–87.

[7] B. Zhou, C. Brackmann, Q. Li, Z. Wang, P. Petersson, Z. Li, M. Aldén, X.-S. Bai, Distributed reactions in highly turbulent premixed methane/air flames. Part I. Flame structure characterization, Combust. Flame 162 (2015), 2937–2953.

[8] M. de Joannon, P. Sabia, G. Sorrentino, A. Cavaliere, Numerical study of mild combustion in hot diluted diffusion ignition (HDDI) regime, Proc Combust. Inst. 32 (2009), 2147–3154.

[9] H. Carlsson, R. Yu, X.-S. Bai, Flame structure analysis for categorization of lean premixed CH4/air and H2/air flames at high Karlovitz numbers: Direct numerical simulation studies, Proc Combust. Inst. 35 (2015), 1425–1432.

[10] C. Duwig, B. Li, Z. S. Li, M. Aldén, High resolution imaging of flameless and distributed turbulent combustion, Combust. Flame 159 (2012), 306–316.

[11] B. Zhou, C. Brackmann, Z. Li, M. Aldén, X.-S. Bai, Simultaneous multi-species and temperature visualization of premixed flames in the distributed reaction zone regime, Proc. Combust. Inst. 35 (2015), 1409–1416.

[12] B. Zhou, Q. Li, Y. He, P. Petersson, Z. Li, M. Aldén, X.-S. Bai, Visualization of multi-regime turbulent combustion in swirl-stabilized lean premixed flames, Combust. Flame 162 (2015), 2954–2958.

[13] B. Zhou, C. Brackmann, Z. Wang, Z. Li, M. Richter, M. Aldén, X.-S. Bai, Thin reaction zone and distributed reaction zone regimes in turbulent premixed methane/air flames: Scalar distributions and correlations, Combust. Flame (2017), 220–236.

[14] K. H. H. Goh, P. Geipel, F. Hampp, R. P. Lindstedt, Regime transition from premixed to flameless oxidation in turbulent JP-10 flames, Proc. Combust. Inst. 34, (2013), 3311–3318.

[15] K. H. H. Goh, P. Geipel, R. P. Lindstedt, Turbulent transport in premixed flames approaching extinction, Proc. Combust. Inst. 35 (2015), 1469–1476.

[16] F. Hampp, R. P. Lindstedt, Strain distribution on material surfaces during combustion regime transitions, Proc. Combust. Inst. 36 (2016), 1911–1918.

[17] F. Hampp, R. P. Lindstedt, Quantification of combustion regime transitions in premixed turbulent DME flames, Combust. Flame 182 (2017), 248–268.

[18] F. Hampp, R. P. Lindstedt, Quantification of external enthalpy-controlled combustion at unity Damköhler number, in A. K. Runchal, A. K. Gupta, A. Kushari, A. De Suresh, K. Aggarwal (eds.) Energy for Propulsion A Sustainable Technologies Approach, Springer Nature Singapore Pte Ltd., (2018), ISBN:978-981-10-7472-1.

[19] F. Hampp, S. Shariatmadar, R. P. Lindstedt, Quantification of low Damköhler number turbulent premixed flames, In press, Proc. Comb. Inst. 37 (2019), 2373–2381.

[20] M. de Joannon, G. Langella, F. Beretta, A. Cavaliere, C. Noviello, Mild Combustion: Process Features and Technological Constrains, Combust. Sci. Technol. 153 (2000), 33–50.

[21] P. Sabia, M. de Joannon, M. L. Lavadera, P. Giudicianni, R. Ragucci, Autoignition delay times of propane mixtures under MILD conditions at atmospheric pressure, Combust. Flame 161 (2014), 3022–3030.

[22] P. Sabia, M. de Joannon, G. Sorrentino, P. Giudicianni, R. Ragucci, Effects of mixture composition, dilution level and pressure on auto-ignition delay times of propane mixtures, Chem. Eng. J. 277 (2015), 324–333.

[23] J. Ye, P. R. Medwell, E. Varea, S. Kruse, B. B. Dally, H. G. Pitsch, An experimental study on MILD combustion of prevaporised liquid fuels, Appl. Energ. 151 (2015), 93–101.

[24] Y. L. Wang, P. S. Veloo, F. N. Egolfopoulos, T. T. Tsotsis, A comparative study on the extinction characteristics of non-premixed dimethyl ether and ethanol flames, Proc Combust. Inst. 33 (2011), 1003–1010.

[25] Y. L. Wang, An experimental and numerical investigation of fundamental combustion properties of biofuels, PhD thesis, University of Southern California, August 2011, url: uscthesesreloadpub_Volume71/etd-WangYangLe-256.pdf .

[26] C. Arcoumanis, C. Bae, R. Crookes, E. Kinoshita, The potential of di-methyl ether (DME) as an alternative fuel for compression-ignition engines: A review, Fuel 87 (2008), 1014–1030.

[27] P. Allison, Y. Chen, J. F. Driscoll, Investigation of Dimethyl Ether Combustion Instabilities in a Partially-Premixed Gas Turbine Model Combustor Using High-Speed Laser Diagnostics, AIAA 52 (2014), DOI: 10.2514/6.2014-0660.

[28] K. Kohse-Höinghaus, P. Oßwald, T. A. Cool, T. Kasper, N. Hansen, F. Qi, C. K. Westbrook, P. R. Westmoreland, Biofuel Combustion Chemistry: From Ethanol to Biodiesel, Angew. Chem. Int. Ed. 49 (2010), 3572–3597.

[29] S.-W. Park, Detailed Chemical Kinetic Model for Oxygenated Fuels, PhD thesis, Imperial College, March 2012, url: http://hdl.handle.net/10044/1/9599.

[30] K. N. C. Bray, Laminar Flamelets and the Bray, Moss, and Libby Model, in N. Swaminathan, K. N. C. Bray (Eds.), Turbulent Premixed Flames, Cambridge University Press, 2011, 41–60, ISBN: 978-0-521-76961-7.

[31] F. Hampp, R. P. Lindstedt, Fractal Grid Generated Turbulence - A Bridge to Practical Combustion Applications, in Y. Sakai and C. Vassilicos (eds.) Fractal Flow Design: How to Design Bespoke Turbulence and why, Springer-Verlag, CISM Int. Mech. Sci. 568, 2016, DOI:10.1007/978-3-319-33310-6 3.

[32] P. Geipel, K. H. H. Goh, R. P. Lindstedt, Fractal-Generated Turbulence in Opposed Jet Flows, Flow Turbul. Combust. 85 (2010), 397–419.

[33] B. Böhm, O. Stein, A. Kempf, A. Dreizler, In-Nozzle Measurements of a Turbulent Opposed Jet using PIV, Flow Turbul. Combust. 85 (2010), 73–93.

[34] K. H. H. Goh, Investigation of Conditional Statistics in Premixed Combustion and the Transition to Flameless Oxidation in Turbulent Opposed Jets, PhD thesis, Imperial College, Aug 2013, url: http://hdl.handle.net/10044/1/28073.

[35] K. H. H. Goh, P. Geipel, R. P. Lindstedt, Lean premixed opposed jet flames in fractal grid generated multiscale turbulence, Combust. Flame 161 (2014), 2419–2434.

[36] D. Geyer, A. Kempf, A. Dreizler, J. Janicka, Turbulent opposed-jet flames: A critical benchmark experiment for combustion LES, Combust. Flame 143 (2005), 524–548.

[37] K. H. H. Goh, P. Geipel, F. Hampp, R. P. Lindstedt, Flames in fractal grid generated turbulence, Fluid Dyn. Res. 45, (2013), 061403.

[38] G. Coppola, A. Gomez, Experimental investigation on a turbulence generation system with high-blockage plates, Exp. Therm. Fluid Sci. 33 (2009), 1037–1048.

[39] F. Hampp, Quantification of Combustion Regime Transitions, PhD thesis, Imperial College, May 2016, url: http://hdl.handle.net/10044/1/32582.

[40] B. Wieneke, K. Pfeiffer, Adaptive PIV with variable interrogation window size and shape, 15^{th} Int. Symp. Appl. Laser Tech. Fluid Mech. (2010), url: http://ltces.dem.ist.utl.pt/LXLASER/lxlaser2010/upload/1845_qkuqls_1.12.3.Full_1845.pdf.

[41] B. Coriton, J. H. Frank, A. Gomez, Effects of strain rate, turbulence, reactant stoichiometry and heat losses on the interaction of turbulent premixed flames with stoichiometric counterflowing combustion products, Combust. Flame 160 (2013), 2442–2456.

[42] M. P. Burke, M. Chaos, Y. Ju, F. L. Dryer, S. J. Klippenstein, Comprehensive H_2/O_2 kinetic model for high-pressure combustion, Int. J. Chem. Kinet., 44 (2012), 444–474.

[43] Y. L. Wang, A. T. Holley, C. Ji, F. N. Egolfopoulos, T. T. Tsotsis, H. J. Curran, Propagation and extinction of premixed dimethyl-ether/air flames, Proc. Combust. Inst. 32 (2009), 1035–1042.

[44] X. Qin, Y. Ju, Measurements of burning velocities of dimethyl ether and air premixed flames at elevated pressures, Proc. Combust. Inst. 30 (2005), 233–240.

[45] J. de Vries, W. B. Lowry, Z. Serinyel, H. J. Curran, E. L. Petersen, Laminar flame speed measurements of dimethyl ether in air at pressures up to 10 atm, Fuel, 90 (2011), 331–338.

[46] T. A. Cool, J. Wang, N. Hansen, P. R. Westmoreland, F. L. Dryer, Z. Zhao, A. Kazakov, T. Kasper, K. Kohse-Höinghaus, Photoionization mass spectrometry and modeling studies of the chemistry of fuel-rich dimethyl ether flames, Proc. Combust. Inst. 31 (2007), 285–293.

[47] J. Wang, M. Chaos, B. Yang, T. A. Cool, F. L. Dryer, T. Kasper, N. Hansen, P. Oßwald, K. Kohse-Höinghaus, P. R. Westmoreland, Composition of reaction intermediates for stoichiometric and fuel-rich dimethyl ether flames: flame-sampling mass spectrometry and modeling studies, Phys. Chem. Chem. Phys. 11 (2009), 1328–1339.

[48] C. K. Law, D. L. Zhu, G. Yu, Propagation and extinction of stretched premixed flames, Proc. Combust. Inst. 21 (1986), 1419–1426.

[49] W. P. Jones, R. P. Lindstedt, The Calculation of the Structure of Laminar Counterflow Diffusion Flames Using a Global Reaction Mechanism, Combust. Sci. Techn. 61 (1988), 31–49.

[50] N. Peters, Kinetic foundation of thermal flame theory, in W. A. Sirignano, A. G. Merzhanov, L. de Luca (Eds.), Advances in Combustion Science: In Honor of Y. B. Zel'dovich, Prog. Astronautics and Aeronautics 173 (1997), 73–91.

[51] J. F. Driscoll, Turbulent premixed combustion: Flamelet structure and its effect on turbulent burning velocities, Prog. Energy Combust. Sci. 34 (2008) pp. 91–134.

[52] E. A. Tingas, D. C. Kyritsis, D. A. Goussis, Autoignition dynamics of DME/air and EtOH/air homogeneous mixtures, Combust. Flame 162 (2015), 3263–3276.

[53] E. A. Tingas, D. C. Kyritsis, D. A. Goussis, Comparative investigation of homogeneous autoignition of DME/air and EtOH/air mixtures at low initial temperatures, Combust. Theor. Model. 21 (2017), 93–119.

[54] C. Ji, C. Liang, Y. Zhu, X. Liu, B. Gao, Investigation on idle performance of a spark-ignited ethanol engine with dimethyl ether addition. Fuel Proc. Technol. 94 (2012), 94–100.

[55] C. K. Westbrook, M. Sjöberg, N. P. Cernansky, A new chemical kinetic method of determining RON and MON values for single component and multicomponent mixtures of engine fuels, Combust Flame 195 (2018), 50–62.

[56] J. Kubesh, S. R. King, W. E. Liss, Effect of gas composition on octane number of natural gas fuels, SAE Technical Paper (1992), 922359.

[57] M. Naito, C. Radcliffe, Y. Wada, T. Hoshino, X. Liu, M. Arai, M. Tamura, A comparative study on the autoxidation of dimethyl ether (DME) comparison with diethyl ether (DEE) and diisopropyl ether (DIPE), J. Loss Prev. Proc. Ind. 18 (2005), 469–473.

[58] C.-C. Chen, H.-J. Liaw, C.-M. Shu, Y.-C. Hsieh, Autoignition Temperature Data for Methanol, Ethanol, Propanol, 2-Butanol, 1-Butanol, and 2-Methyl-2,4-pentanediol, J. Chem. Eng. Data 55 (2010), 5059–5064.

[59] C. Robinson, D. B. Smith, The auto-ignition temperature of methane, J. Hazard. Mat. 8 (1984), 199–203.

[60] I. G. Shepherd, R. K. Cheng, P. J. Goix, The spatial scalar structure of premixed turbulent stagnation point flames, Proc. Combust. Inst. 23 (1991), 781–787.

[61] A. M. Steinberg, J. F. Driscoll, S. L. Ceccio, Measurements of turbulent premixed flame dynamics using cinema stereoscopic PIV, Exp. Fluids 44 (2008), 985–999.

[62] B. E. Battles, R. K. Hanson, Laser-induced fluorescence measurements of NO and OH mole fraction in fuel-lean, high-pressure (1–10 atm) methane flames: Fluorescence modeling and experimental validation, J. Quant. Spectrosc. Radiat. Transfer 54 (1995), 521–537.

[63] B. Böhm, C. Heeger, I. Boxx, W. Meier, A. Dreizler, Time-resolved conditional flow field statistics in extinguishing turbulent opposed jet flames using simultaneous highspeed PIV/OH-PLIF, Proc. Combust. Inst. 32 (2009), 1647–1654.

[64] K. A. Buch, W. J. A. Dahm, Experimental study of the fine-scale structure of conserved scalar mixing in turbulent shear flows. Part 2. Sc = 1, J. Fluid Mech. 364 (1998), 1–29.

[65] G. K. Batchelor, Small-scale variation of convected quantities like temperature in turbulent fluid Part 1. General discussion and the case of small conductivity, J. Fluid Mech. 5 (1959), 113–133.

[66] I. G. Shepherd, J. B. Moss, K. N. C. Bray, Turbulent transport in a confined premixed flame, Proc. Combust. Inst. 19 (1982), 423–431.

[67] C. J. Lawn, R. W. Schefer, Scaling of premixed turbulent flames in the corrugated regime, Combust. Flame 146 (2006), 180–199.

[68] H. Shen, J. A. Sutton, A Comparison of the Reactive OH Layer Structure between CH4- and DME-Based Turbulent Non-premixed Jet Flames, 8th National Combustion Meeting, Park City, Utah, May 2013.

[69] Z. Chen, X. Qin, Y. Ju, Z. Zhao, M. Chaos, F. L. Dryer, High temperature ignition and combustion enhancement by dimethyl ether addition to methane-air mixtures, Proc Combust. Inst. 31 (2007), 1215–1222.

[70] F. Herrmann, B. Jochim, P. Oßwald, L.Cai, H. Pitsch, K. Kohse-Höinghaus, Experimental and numerical low-temperature oxidation study of ethanol and dimethyl ether, Combust. Flame 161 (2014), 384–397.

[71] E. Mastorakos, A. M. K. P. Taylor, J. H. Whitelaw, Extinction of Turbulent Counterflow Flames with Reactants Diluted by Hot Products, Combust. Flame 102 (1995), 101–114.

[72] N. Chakraborty, N. Swaminathan, Influence of the Damköhler number on turbulence-scalar interaction in premixed flames. I. Physical insight, Phys. Fluids 19 (2007), 045103.

Figures

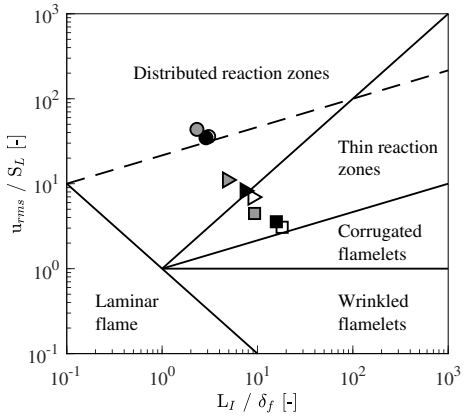

Figure 1: Combustion regime transitions of DME, EtOH and CH_4 visualised in a Borghi diagram for varying Φ. Empty symbols are the DME cases, filled EtOH and grey CH_4. ○: $\Phi = 0.20$, ▷: $\Phi = 0.60$, □: $\Phi = 1.0$.

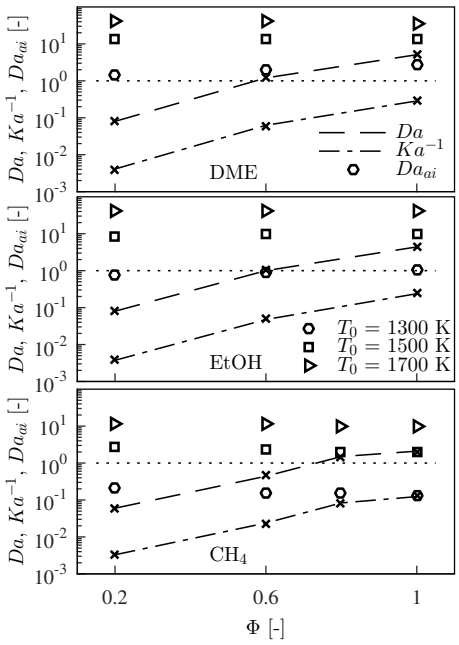

Figure 2: Estimated transition from conventional flame propagation (indicated by means of Da and Ka^{-1}) to an auto-ignition related burning mode (Da_{ai}) for DME (top), EtOH (middle) and CH_4 (bottom). The markers indicate the three Da_{ai} evaluated at initial temperatures of 1300, 1500 and 1700 K.

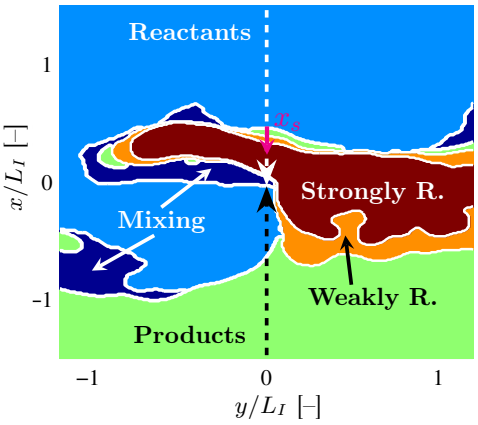

Figure 3: Instantaneous quinary multi-fluid field for DME / air at $\Phi = 0.60$ with T_{HCP} = 1700 K truncated around the stagnation point. Vertical white/black arrows show the theoretical stagnation point streamline (SPS). Interfaces are defined by the intersection of the SPS and material surfaces (white iso-contours). Reactants (light blue); Mixing (blue); Weakly reacting (orange); Strongly reacting (red); Products (green). The magenta arrow shows the x_s origin.

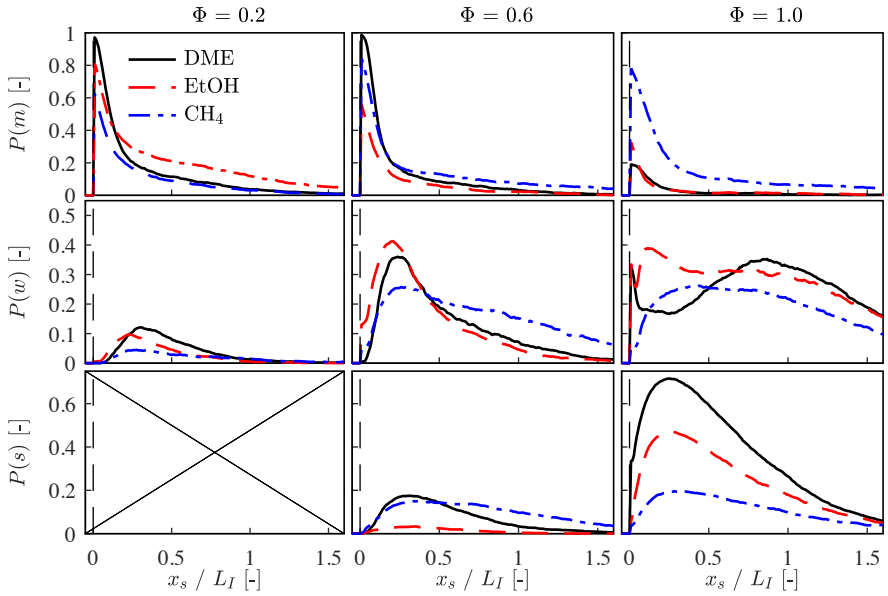

Figure 4: Multi-fluid probability (P) statistics for DME, EtOH and CH_4 combustion with varying Φ along the stagnation point streamline with data aligned at the $x_s = 0$ iso-contour. Top row: Mixing fluid probability ($P(m)$); Middle row: Weakly reacting fluid probability ($P(w)$); Bottom row: Strongly reacting fluid probability ($P(s)$); First column: $\Phi = 0.20$; Second column: $\Phi = 0.60$; Third column: $\Phi = 1.0$.

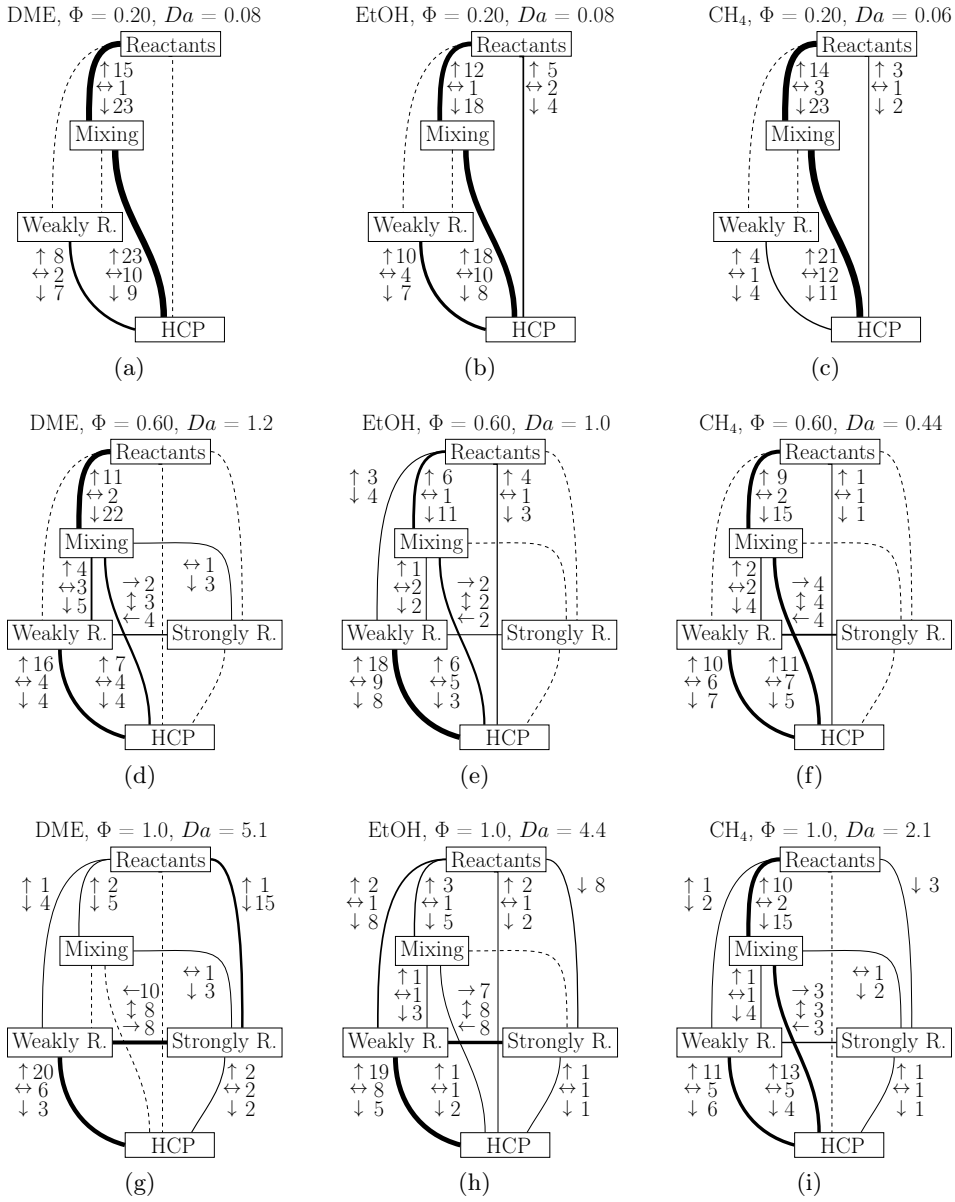

Figure 5: Fuel comparison by means of multi-fluid interface statistics in percent based on the total number of interfaces (N_i) where arrows indicate cases where (i) $\uparrow$ the streamline tangent ($\hat{\mathbf{s}}$:= positive in flow direction) and interface normal ($\hat{\mathbf{n}}$:= positive from reactants to products) are aligned, i.e. $\hat{\mathbf{s}} \cdot \hat{\mathbf{n}} > 0.31$, (ii) $\leftrightarrow$ nearly tangential flow, i.e. $||\hat{\mathbf{s}} \cdot \hat{\mathbf{n}}|| < 0.31$ (i.e. $72 - 108°$) and (iii) $\downarrow$ the opposite of (i) with $\hat{\mathbf{s}} \cdot \hat{\mathbf{n}} < -0.31$ for all cases.

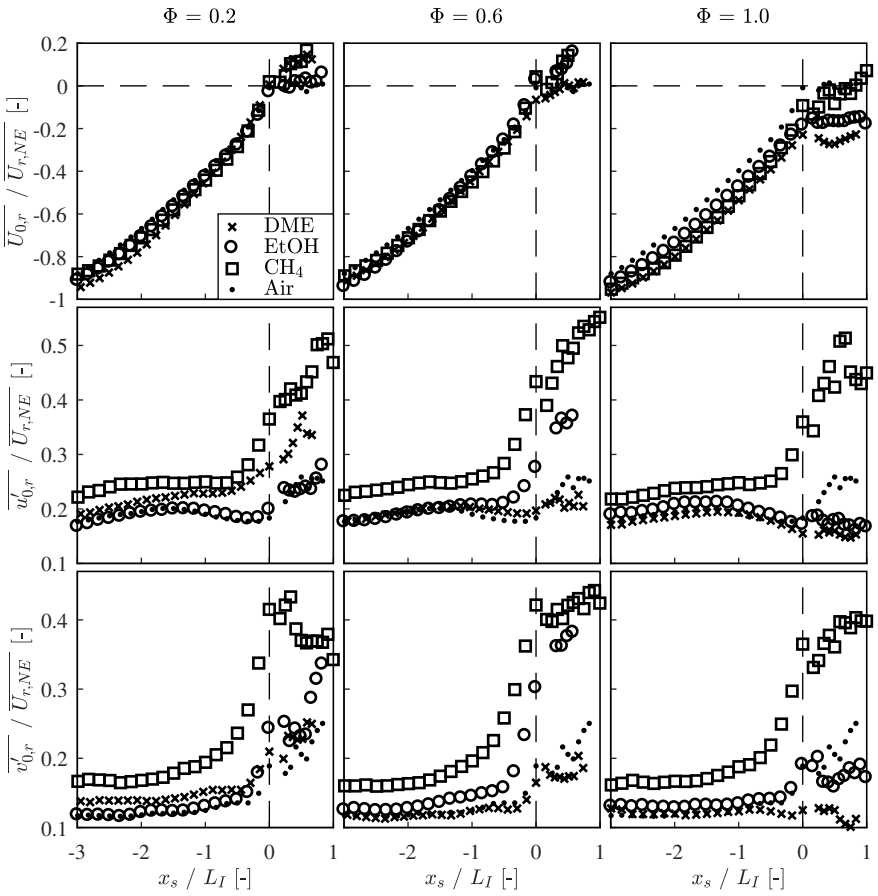

Figure 6: Conditional mean axial reactant fluid velocity and the axial and radial fluctuation for DME, EtOH and CH_4 at varying Φ evaluated along the stagnation point streamline and aligned at $x_s = 0$. The dotted line indicates the mixing case (i.e. air with $\Phi = 0.0$) for reference. Top row: $\overline{U_{0,r}}$ / $\overline{U_{r,NE}}$; Middle row: $\overline{u'_{0,r}}$ / $\overline{U_{r,NE}}$; Bottom row: $\overline{v'_{0,r}}$ / $\overline{U_{r,NE}}$; First column: $\Phi = 0.20$; Second column: $\Phi = 0.60$; Third column: $\Phi = 1.0$.

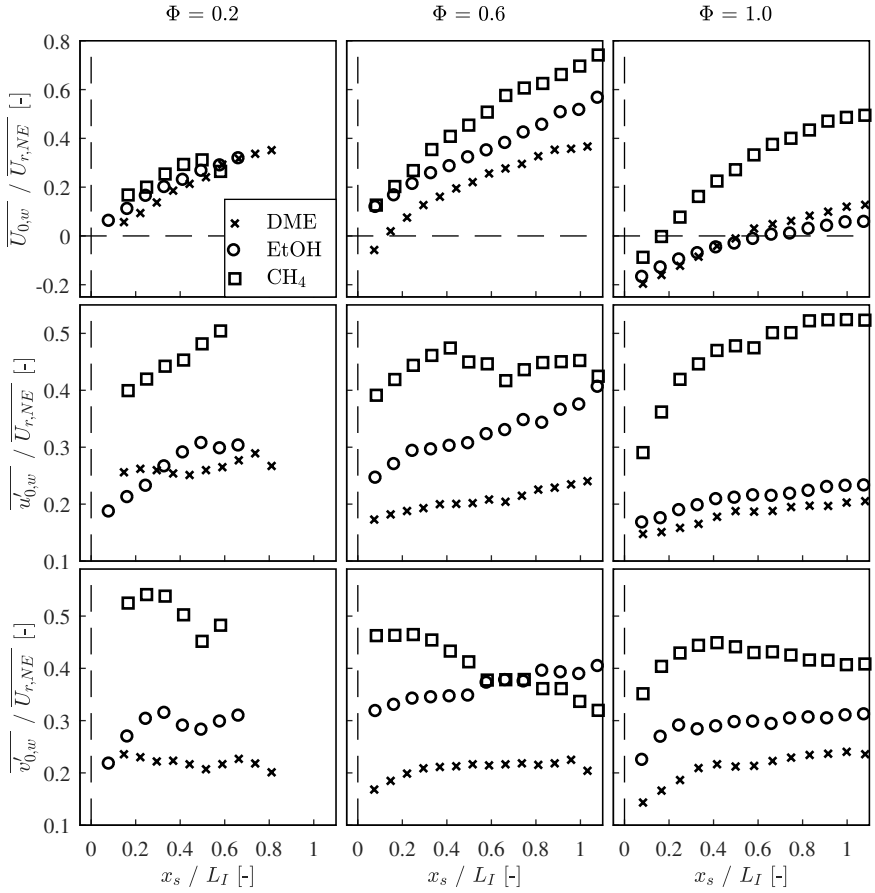

Figure 7: Conditional mean axial weakly reacting fluid velocity and the axial and radial fluctuations for DME, EtOH and CH_4 at varying Φ evaluated along the stagnation point streamline and aligned at $x_s = 0$. Top row: $\overline{U_{0,w}}$ / $\overline{U_{r,NE}}$; Middle row: $\overline{u'_{0,w}}$ / $\overline{U_{r,NE}}$; Bottom row: $\overline{v'_{0,w}}$ / $\overline{U_{r,NE}}$; First column: $\Phi = 0.20$; Second column: $\Phi = 0.60$; Third column: $\Phi = 1.0$.

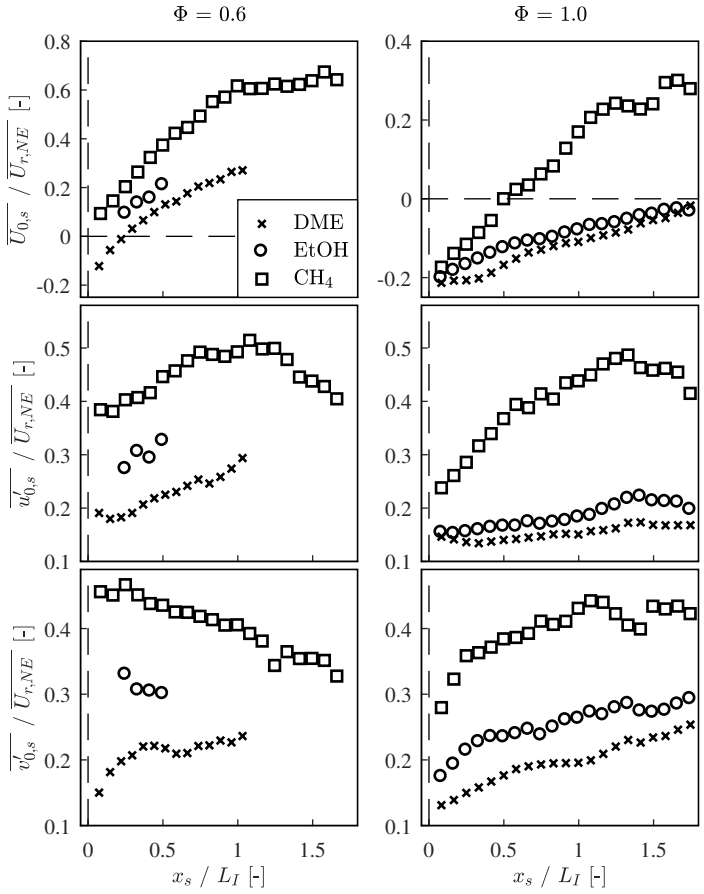

Figure 8: Conditional mean axial strongly reacting fluid velocity and the axial and radial fluctuations for DME, EtOH and CH_4 at varying Φ evaluated along the stagnation point streamline and aligned at $x_s = 0$. Top row: $\overline{U_{0,s}}$ / $\overline{U_{r,NE}}$; Middle row: $\overline{u'_{0,s}}$ / $\overline{U_{r,NE}}$; Bottom row: $\overline{v'_{0,s}}$ / $\overline{U_{r,NE}}$; First column: $\Phi = 0.60$; Second column: $\Phi = 1.0$.

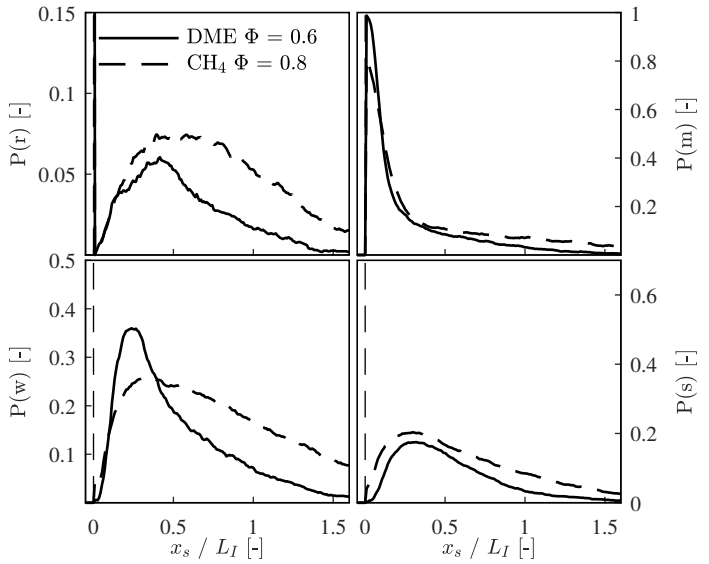

Figure 9: Conditional multi-fluid probabilities for cases with similar Damköhler numbers ($Da = 1.2$ vs. 1.5; DME with $\Phi = 0.60$ vs. CH_4 with $\Phi = 0.80$). Top left: Reactant fluid probability $P(r)$; Top right: Mixing fluid probability $P(m)$; Bottom left: Weakly reacting fluid probability $P(w)$; Bottom right: Strongly reactant fluid probability $P(s)$.

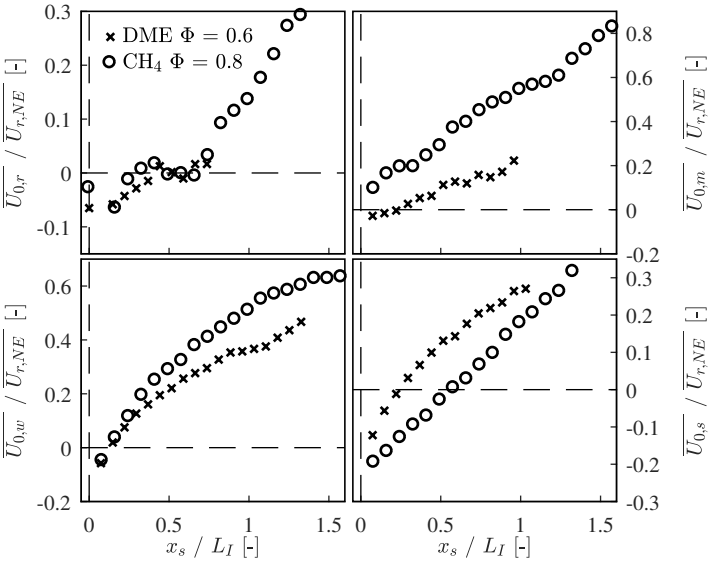

Figure 10: Conditional mean axial fluid velocities for cases with similar Damköhler numbers ($Da = 1.2$ vs. 1.5; DME with $\Phi = 0.60$ vs. CH_4 with $\Phi = 0.80$). Top left: Reactant fluid velocity; Top right: Mixing fluid velocity; Bottom left: Weakly reacting fluid velocity; Bottom right: Strongly reactant fluid velocity.

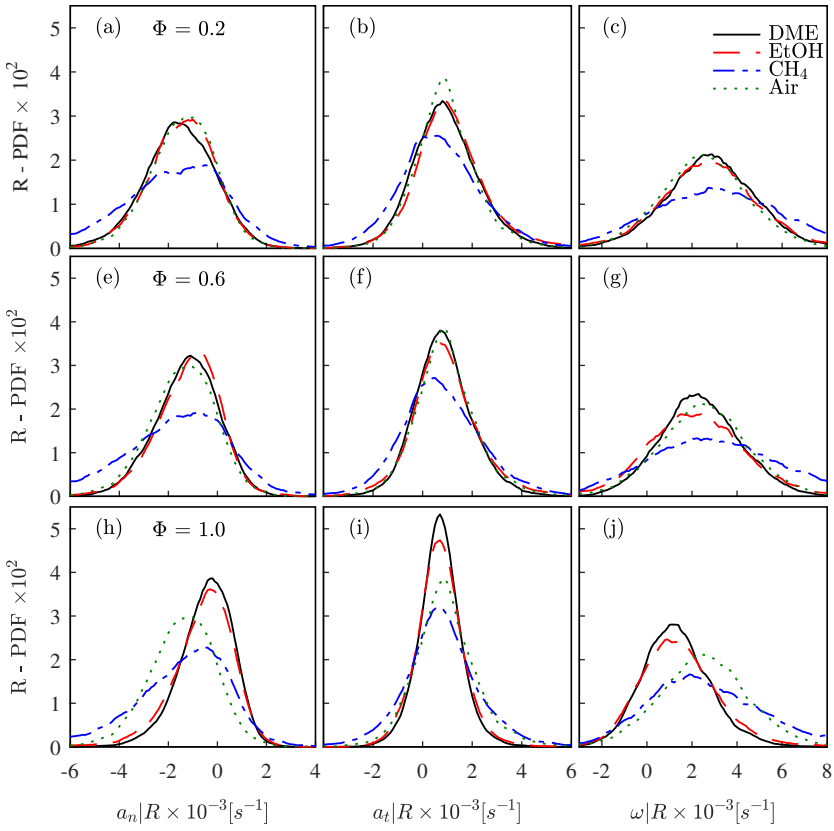

Figure 11: PDF of the rate of strain along the reactant fluid surface (R) for DME, EtOH and CH_4 at varying Φ. The dotted line indicates the mixing case (i.e. air with $\Phi = 0.0$) for reference. First column: Normal strain; Second column: Tangential strain; Third column: Vorticity. First row: $\Phi = 0.20$; Second row: $\Phi = 0.60$; Third row: $\Phi = 1.0$.

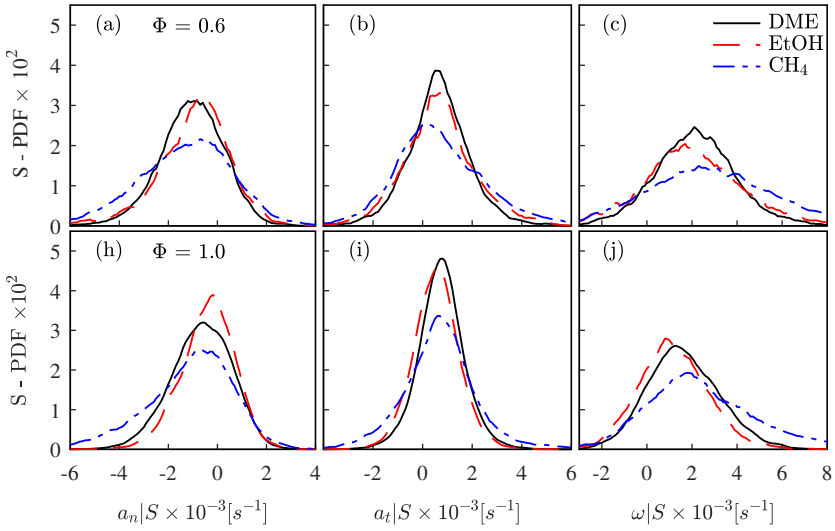

Figure 12: PDF of the rate of strain along the strongly reacting fluid surface (S) for DME, EtOH and CH_4 at varying Φ: First column: Normal strain; Second column: Tangential strain; Third column: Vorticity. First row: $\Phi = 0.60$; Second row: $\Phi = 1.0$.